Elucidating Molecular Mechanisms of Protoxin-2 State-specific Binding to the Human $Na_V1.7$ Channel

Khoa Ngo*[1,2], Diego Lopez Mateos*[1,2], Kyle Rouen[1,2], Yanxiao Han[2], Heike Wulff[3], Colleen E. Clancy**[2,3], Vladimir Yarov-Yarovoy**[2,4], and Igor Vorobyov**[2,3]

[1]Biophysics Graduate Group, [2]Department of Physiology and Membrane Biology, [3]Department of Pharmacology and [4]Department of Anesthesiology and Pain Medicine; University of California, Davis

** These authors contributed equally*

***Correspondence to Colleen E. Clancy (ceclancy@ucdavis.edu), Vladimir Yarov-Yarovoy (yarovoy@ucdavis.edu), and Igor Vorobyov (ivorobyov@ucdavis.edu)*

Running title: Protoxin-2 - $Na_V1.7$ channel state-specific binding

Abstract:
Human voltage-gated sodium (hNa_V) channels are responsible for initiating and propagating action potentials in excitable cells and mutations have been associated with numerous cardiac and neurological disorders. $hNa_V1.7$ channels are expressed in peripheral neurons and are promising targets for pain therapy. The tarantula protoxin-2 (PTx2) has high selectivity for $hNa_V1.7$ and serves as a valuable scaffold to design novel therapeutics to treat pain. Here, we used computational modeling methods to study the molecular mechanisms by which PTx2 exhibits state-dependent binding to $hNa_V1.7$ voltage-sensing domains (VSDs). Using Rosetta structural modeling methods, we constructed atomistic structural models of the $hNa_V1.7$ VSD II and IV in the activated and deactivated states with docked PTx2. We then performed microsecond-long all-atom molecular dynamics (MD) simulations of the systems in hydrated lipid bilayers. Our simulations revealed that PTx2 binds most favorably to VSD II and IV in the deactivated conformations. These state-specific interactions are mediated primarily by PTx2 R22, K26, and K27 residues with the VSD S3-S4 loop, and L23, W24 with the S1-S2 loop. The surrounding membrane lipids facilitated the binding process. Our work revealed important protein-protein contacts that contribute to high-affinity state-dependent toxin interaction with the channel. The workflow presented will prove useful for designing novel peptides with improved selectivity and potency for more effective and safe treatment of pain.
Summary: Voltage-gated sodium channel $Na_V1.7$ plays a major role in pain perception and is selectively inhibited by tarantula venom protoxin-2, used to design pain therapeutics. Here, Ngo *et al* applied computational modeling to assess state-dependent protoxin-2 – $Na_V1.7$ binding.
Keywords: Voltage-gated sodium channel, peptide toxin, Rosetta structural modeling, molecular docking, molecular dynamics simulation

1. Introduction

Voltage-gated sodium (Na_V) channels are responsible for electric signaling and play a key role in various physiological processes[1,2]. Na_V channels are involved in the functioning of the central and peripheral nervous systems and the contraction of skeletal and cardiac muscles[2]. There are nine known members in the Na_V family, named $Na_V1.1$ to $Na_V1.9$[2]. A eukaryotic Na_V channel is composed of four homologous domains (DI-DIV), each containing six transmembrane segments (S1-S6), with

S1 through S4 serving as the voltage-sensing domain (VSD). The S4 segment contains four or five positively charged amino acid residues acting as voltage sensors. The S5 and S6 segments, along with intervening loops and pore helix form the channel pore, which contains the ion selectivity filter (SF) region. Membrane depolarization induces the charged residues in the S4 segment to move outwards, a movement that is transmitted to the pore domain through the S4-S5 linker leading to channel opening and a rapid influx of sodium ions into the cell. This sodium influx further depolarizes the cell membrane and leads to the generation of an action potential. The opening of the Na_V channels is dependent on the sequential activation of VSD I through III[3,4]. In contrast, the activation of VSD IV is coupled with the rapid inactivation of the channel through the release of the IFM motif (inactivation gate)[3–6]. This inactivation process is crucial to stop the influx of sodium ions and enable the repolarization of the membrane to conclude the action potential.

Na_V channel dysfunctions arising from mutations can lead to various pathophysiological conditions including arrhythmias, epilepsy, chronic pain, and insensitivity to pain[7]. $Na_V1.3$, $Na_V1.7$, $Na_V1.8$, and $Na_V1.9$ channels have been implicated in pain signaling[2]. Transgenic mice lacking $Na_V1.7$- and $Na_V1.8$-positive nociceptors have been shown in experiments to exhibit increased mechanical and thermal pain thresholds[8]. In particular, the mice showed reduced or no response to inflammatory pain responses evoked by various stimuli[8]. Additionally, individuals born with loss-of-function mutations in the SCN9A gene encoding for the $Na_V1.7$ α subunit were discovered to have congenital insensitivity to pain. In contrast, gain-of-function mutations were associated with aberrant chronic pain sensation and related disorders such as inherited erythromelalgia and paroxysmal extreme pain disorder[9,10]. These observations further emphasize the importance of the $Na_V1.7$ channels to pain perception.

Local anesthetics, such as lidocaine, are used to reduce the transmission of pain signals to the central nervous system by non-selectively blocking various Na_V subtypes[11]. Due to the local anesthetics' lack of Na_V selectivity, side effects are often reported concerning the loss of other sensations, such as the sense of touch. Use of opioid analgesics is associated with side effects such as respiratory depression, constipation, and development of dependence[12]. Therefore, developing drugs that selectively inhibit $Na_V1.7$ function may result in strong analgesia without undesirable side effects[13,14]. Na_V channels implicated in pain signaling have been discovered to be targets of natural toxins found in species such as spiders and scorpions[7]. The toxins modulate channel activity by either blocking the ion permeation pathway (i.e., pore blockers) or binding to VSD to alter channel gating kinetics (i.e., gating modifier toxins, or GMTs)[15].

Protoxin-2 (PTx2), a 30 amino acid residue peptide derived from the venom of the *Peruvian Green Velvet* tarantula, has a moderate selectivity for $Na_V1.7$ versus other Na_V, thus making it a suitable scaffold for a peptide-based pain therapeutic[16]. This toxin interferes with the activation of Na_V channels by binding to the S3-S4 loop in VSD II and shifting the voltage dependence of activation to a more positive potential[16]. PTx2 is 100-fold more potent for $Na_V1.7$ (IC_{50} = 0.3-1.0 nM) versus other Na_V subtypes[13,17–19]. Additionally, PTx2 binds to deactivated $hNa_V1.7$ VSD IV inhibiting fast inactivation and producing sustained sodium currents, similar to the effect of α-scorpion toxins, but with lower potency (IC_{50} = 0.24 μM)[18]. However, this effect of PTx2 is typically masked by the preferential inhibition of Na_V channel activation due to higher affinity binding to VSD II[18].

By using peptide toxins as a scaffold for designing novel pain treatments, researchers can develop more effective and targeted therapies for chronic pain[14,20]. Additionally, molecular probes based on peptide toxins can be effective tools to study the mechanisms and dynamics of ion channels[21,22]. Understanding the molecular mechanisms of PTx2 interaction with hNav1.7 is essential to understand the toxin's potency and selectivity, the molecular basis of its gating modification effects, and ultimately, to create new peptides with improved properties. However, structural determination of toxins bound to $hNa_V1.7$ in different states has been hampered by the technical difficulties in purifying and crystallizing the fully human $Na_V1.7$, which was accomplished only recently by *Shen et al.* using cryogenic electron microscopy (cryo-EM) and resulted in the generation of several channel structures including one with bound PTx2 to activated VSD II and VSD IV (PDB: 6J8J[16]). However, the PTx2 binding mechanisms are obscure from such structures and other peptide toxin-ion channel complexes since the bound toxin interactions are not well resolved in the low-resolution PTx2 densities in the cryo-EM $hNa_V1.7$ structures. Moreover, stabilizing VSDs in a deactivated state is challenging without a lipid bilayer and applied membrane voltage. To overcome the technical hurdles of working with the fully human $Na_V1.7$, several groups have engineered chimeric constructs in which part of the $hNa_V1.7$ sequence is grafted into another ion channel. *Xu et al*. replaced the top part of the VSD of the homotetrameric prokaryotic Na_VAb channel with the corresponding amino acid sequence from $hNa_V1.7$ VSD II[23]. The chimeric $hNa_V1.7$-VSD II-Na_VAb channel retained the ability to bind PTx2 and resulted in the X-ray structure of PTx2-$hNa_V1.7$-VSD II-Na_VAb complex with the VSD in the activated state (PDB: 6N4I[23]). Using the same chimeric construction, the same authors obtained the cryo-EM structures of the PTx2-$hNa_V1.7$-VSD II-Na_VAb complex in the activated (PDB: 6N4Q[23]) and deactivated (PDB: 6N4R[23]) states.

Potential strategies to for pain therapy via $hNa_V1.7$ gating inhibition can include the trapping of VSD II in the deactivated state (to prevent the channel from activating) or of VSD IV in the activated state (to keep the channel in the inactivated, non-conducting state). However, current structural studies have not yet resulted in a complete atomic-resolution understanding of how PTx2 interacts with $Na_V1.7$ VSDs in a state-specific manner and did not provide energetic and dynamic insights into toxin-channel interactions, which are crucial to designing improved peptides as ion channel modulators. Computational techniques can provide important insights into the atomic-level mechanisms involved in ion channel function and modulation[24] and toxin binding[25–27] Moreover, they are useful tools to guide the peptide design process towards enhanced toxin variants[13,28]. In our study, we demonstrated that computational structural modeling and molecular dynamics simulations could accurately capture the atomic-resolution molecular mechanisms by which PTx2 binds to $hNa_V1.7$ VSD II and IV in the activated and deactivated states (transmembrane helix S4 in the "up" or "down" state, respectively, as shown in **Figure 1**). Our molecular modeling and simulation insights will be useful to inform future peptide design studies and help researchers to identify potential toxin peptide mutations to improve PTx2 selectivity and potency for $hNa_V1.7$. Moreover, our methodology can be expanded to study other toxin-channel interactions to design potential treatments for diseases such as cardiac arrhythmia, epilepsy, neuropathic pain, and other neurological disorders[29].

2. Materials and methods

2.1 Structural modeling and peptide docking

In this study, we used computational modeling techniques and structural data to investigate the atomic-scale interaction mechanisms between PTx2 and the VSDs of $hNa_V1.7$ in multiple states (**Figure 1**). Our primary objective was to generate models of PTx2 bound to VSD II and VSD IV in deactivated and activated conformations as input for molecular dynamics (MD) simulations.

To achieve this goal, we first employed cryo-EM structures of PTx2 bound to $hNa_V1.7$ to both the activated VSD II and VSD IV (PDBs: 6J8J[16]). However, the resolution of the toxin EM density, at ~5 Å, did not permit complete atomic structure reconstruction in the experimental structure[16]. To overcome this limitation, we utilized the Rosetta structural modeling software suite[30] and the experimental EM density data to model the interactions of PTx2 with activated $hNa_V1.7$ VSD II and VSD IV. For VSD II, we also had to use Rosetta Loop Modeling[31,32] for missing residues in the S3-S4 loop which are key in interacting with PTx2 based on experimental data[23].

The PTx2 docking protocol comprised a first step using RosettaDock[33,34] with Rosetta membrane energy function[35]. In this step, the channel was transformed into membrane coordinates by superimposing it into a reference $hNa_V1.7$ experimental structure downloaded from the PDBTM database (which stores experimental structures of membrane proteins in membrane coordinates). The toxin was placed manually in three different initial locations around the binding site in the corresponding VSD, using the toxin's EM density as a reference. Subsequently, 20,000 docked models per input were generated, with RosettaDock making a total of 60,000 models. Top 10% of models based on Rosetta total_score (total computed Rosetta energy of the protein) was extracted, and the top 100 interface_score (Rosetta interaction energy) models were used as input for the next step. The second step involved EM density fitting of top-docked models to the experimental EM map using Rosetta EM density refinement[36]. In this step, 500 models were generated per input making a total of 50,000 models. The top 10% of models based on total_score was initially extracted. Final models were selected based on the recalculated interface_score after EM fitting, and on the elec_dens_fast score term (agreement between the Rosetta model and the experimental EM maps). Although the whole channel was present during the docking simulations, we removed everything except the corresponding VSD and PTx2 before proceeding to the MD simulations to save computational resources.

Furthermore, we docked PTx2 onto the structure of $hNa_V1.7$ VSD IV trapped in a deactivated state by an α-scorpion toxin (PDB: 6NT4[4]), thereby constructing a model of PTx2 bound to deactivated $hNa_V1.7$ VSD IV. Note that this experimental structure comprises a human-cockroach chimeric ion channel, in which the VSD IV displays a human sequence while the remaining part is derived from the Na_V-PaS channel. To model the interactions between PTx2 and VSD IV, the Na_V-PaS portion was removed, leaving only the VSD. The docking protocol was similar to the two cases above, but without any EM density-related refinement or scoring, since there is no experimental map available for this interaction. Finally, we employed the Cryo-EM structure of the chimera channel $hNa_V1.7$-VSD II-NaVAb (PDB: 6N4R[23]), which has the VSD in a deactivated conformation, as a template for RosettaCM[37] (homology modeling). This allowed us to generate a model of the deactivated VSD II with the entire $hNa_V1.7$ VSD II sequence (sequence identity between template and target: 63.7%). We generated 5,000 RosettaCM models, extracted the top 10% based on total_score, and selected the final model based on both low RMSD for the template and low total_score. Then, we utilized

RosettaDock[33,34] with a membrane energy function[35] to dock PTx2 to the deactivated VSD II of hNa$_V$1.7 as described above.

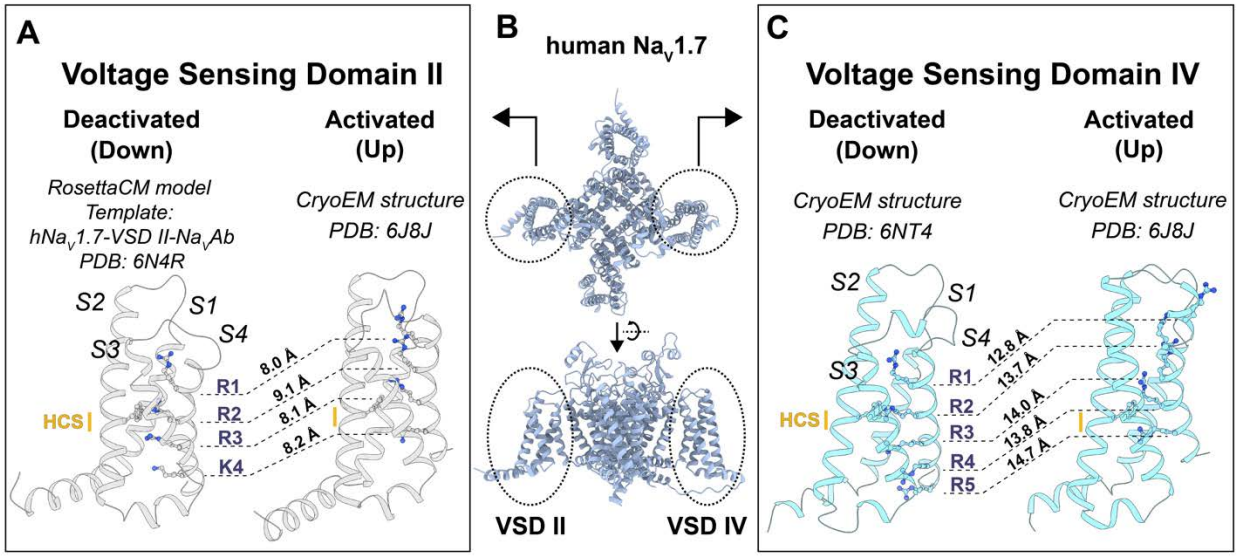

Figure 1. ***Structural comparison of different conformational states of hNa$_V$1.7 VSD II and IV.*** *A) Snapshots of deactivated (left) and activated (right) VSD II structures. For each state, S1 to S4 VSD segments are shown, highlighting the gating charge residues ("R1", "R2", "R3", "K4", "R5") and the hydrophobic constriction site (HCS) in yellow. The distance between the C$_\alpha$ atoms of each gating charge in each state after superimposition of the VSDs is shown. B) Global view of cryo-EM Na$_V$1.7 structure from PDB 6J8J[16] highlights the VSD II and IV positions. C) Snapshots of deactivated (left) and activated (right) VSD IV structures (same information as in A).*

2.2 Atomistic MD simulations

Using the CHARMM-GUI web server[38], the VSD-bound-toxin complexes were inserted into tetragonal phospholipid bilayer patches composed of 160 1-palmitoyl-2-oleoylphosphatidylcholine (POPC) molecules. The systems were then solvated by a 0.15 M aqueous NaCl solution to mimic physiological extracellular environment, resulting in molecular systems of ~63,000 atoms. All-atom molecular dynamics (MD) simulations were then performed with Amber20[39] using the standard CHARMM36m all-atom force field for protein, lipid, ions[40–42], and TIP3P water model[43]. The system then underwent an MD equilibration protocol during which a 1 kcal/mol/Å^2 harmonic restraint was initially applied to all atoms in the system and then gradually reduced to 0.1 kcal/mol/Å^2 over a period of 90 ns. A production run then commenced for another 910 ns (totaling 1 μs of simulation time), during which a weak 0.1 kcal/mol/Å^2 harmonic restraint was imposed on C$_\alpha$ atoms of the VSD transmembrane helices S1-S4 to alleviate potential structural instability that might be caused by the isolation of the VSD from the full channel.

Subsequently, protein-ligand interactions were characterized in each set of simulations using in-house Python scripts incorporating the protein–ligand interaction profiler (PLIP) Python module[44]. Binding free energy calculations were performed using the Molecular Mechanics Poisson-Boltzmann

Surface Area (MM/PBSA) approach[45–47] with all-atom simulation trajectories by MMPBSA.py program in Amber Tools[48]. The Chamber module of ParmEd program was used to convert CHARMM-style forcefields to Amber-style forcefield[49]. The aqueous solution (with ionic strength of 150 mM) and lipid membrane were treated implicitly using dielectric constants, denoted ε (water $\varepsilon_w = 80$, lipid bilayer $\varepsilon_l = 2$ and protein $\varepsilon_p = 4$). Solvent probe radius was set to 1.4, and the atomic radii were set according to the converted force field parameters. To obtain the solvation-free energy and the gas phase energy contributions without entropy, the particle-particle particle-mesh (P3M) procedure was used[50]. These calculations above were performed with implicit membrane, where the electrostatic energy includes both reaction filed and Coulombic electrostatic energies. Entropy was calculated separately by the interaction entropy method[51], where interaction energy between PTx2 and $hNa_V1.7$ VSD II/IV including only Coulombic electrostatic and van der Waals energies was needed. To obtain the Coulombic energy separated from the reaction field energy, each system energy was recalculated using the dielectric boundary surface charges method in the implicit ionic solution.

However, to calculate the energy contribution of each residue to the binding process for each system, we employed the Molecular Mechanics/Generalized Born Surface Area (MM/GBSA) approach[52] as non-polar solvation energies are not decomposable with Poisson-Boltzmann implicit solvent model associated with MM/PBSA. The binding free energy of each residue is computed by summing the van der Waals contribution from molecular mechanics, electrostatic energy, electrostatic contribution to the solvation free energy calculated by GB, and polar and non-polar contributions to the solvation free energy. MM/GBSA calculations were performed in an aqueous solution with ionic strength of 150 mM. As membrane was neither incorporated implicitly nor explicitly in our MM/GBSA binding free energy calculations, we computed the electrostatic and van der Waals interaction energies of PTx2 with POPC lipids and VSD II/IV using AMBER linear interaction energy analysis[39,53].

2.3 Molecular graphics

Molecular graphics visualization was performed using UCSF ChimeraX[54] to depict all resulting models and illustrate residue interactions. Structural comparison was carried out through the superposition of the structures using the MatchMaker tool within ChimeraX.

2.4 Supplementary information

Supplementary information (SI) includes: 1) Ptx2, $hNa_V1.7$ VSD II and VSD IV amino acid sequences used in this study; 2) SI Figures S1-S11 detailing specific Ptx2 - $hNa_V1.7$ VSD inter-residue interactions including their frequencies and interaction energies; 3) two SI videos demonstrating structural transitions of Ptx2 - $hNa_V1.7$ VSD II and VSD IV complexes between deactivated and activated VSD states using RosettaDock models.

2. Results

3.1 General overview of different docked structures

While experimental structures of activated and deactivated VSD IV and activated VSD II are available, the experimental structure of deactivated VSD II of hNaV1.7 has yet to be determined. To acquire the necessary structural information, we sought to obtain structures of both $hNa_V1.7$ VSD II and VSD IV in both activated and deactivated conformations. To obtain a structure of deactivated VSD II, we used

the experimental structure of the hNa$_V$1.7-VSD II-Na$_V$Ab chimera (PDB: 6N4R[23]) as a template for homology modeling using the RosettaCM software[37] (sequence identity: 63.7%). We then compared the positions of gating charges in each VSD by calculating the distances between equivalent C_α atoms after VSD superimposition (**Figure 1**). Our analysis revealed that gating charges of VSD II move ~8.5 Å, on average, between the deactivated and activated states. In the deactivated state, only the first gating charge ("R1") is above the hydrophobic constriction site (HCS), while in the activated state "R1", "R2" and "R3" are above the HCS. VSD IV showed a more dramatic displacement of the gating charges (~13.8 Å) between the activated and deactivated states. Just as in VSD II, in the deactivated conformation, only "R1" is located above the HCS; however, in the activated conformation of VSD IV "R4" also reaches above the HCS, which contrasts with the activated VSD II structure where only "R1" to "R3" lie above the HCS. These results suggest that the VSD II in the Na$_V$1.7 cryo-EM structure (PDB: 6J8J[16]) is not fully activated, which might be explained by the presence of PTx2 or the lack of membrane voltage during the structure determination process.

Subsequently, structural models of PTx2 in complex with VSD II and VSD IV were generated in both deactivated and activated states as starting points in MD simulations. The methodology utilized for the generation of these models is outlined in **Figure 2** and briefly summarized as follows: RosettaDock with a membrane energy function was employed for docking PTx2 to the VSDs. The activated conformations of the VSDs (PDB: 6J8J)[16] with PTx2 were further refined using the available experimental EM density maps (refer to the Methods section for further details).

PTx2 interferes with Na$_V$1.7 activation by binding potently (IC_{50} = 0.3-1.0 nM) to the S3-S4 loop in VSD II and shifting the voltage dependence of activation to more depolarized potentials[13,16–19]. Analysis of the structural models provided important insights into the conformational-dependent binding of PTx2 to Na$_V$1.7 VSD II & VSD IV. PTx2 binds to the VSD II at the "LFLAD" motif, which comprises residues L812 to D816 and is located within the S3 segment and S3-S4 loop[23]. The toxin binding interface can be divided into two distinct regions: polar and hydrophobic. In the polar interface of the PTx2 - deactivated VSD II model (**Figure 3A, panel i**), the first gating charge ("R1") is observed to be located below the channel-toxin interface. The electronegative pocket created by E811 and D816 forms hydrogen bonds and salt bridges with the positively charged toxin residues K26 and R22 (**Figure 3A, panel iii**). The hydrophobic interface (**Figure 3A, panel ii**) is composed of M6 and tryptophan residues W5, W24, and W30 from the toxin and L812 and F813 from the channel S3 segment. Additionally, W24 was observed to be positioned into the VSD top wedge, making hydrophobic contacts with channel residues A776 and L770 from VSD II segment S2 (Figure 4A, panel iv). In the PTx2 – activated VSD II model (**Figure 3B**), the upward movement of the S4 segment and subsequent relocation of the "R1" gating charge residue disturbs the electronegative pocket, and the toxin experiences a global shift that pulls it away from the VSD (**Supplementary Video 1**). The main interaction in our PTx2 – activated VSD II model at the polar interface is between toxin R22 and K26 residues and channel D816 residue (**Figure 3B, panel iii**). E818 interacts with K28 from the channel, although this interaction is not present in any of the experimental structures. The hydrophobic interface (**Figure 3B, panel ii**) comprises π-stacking interactions between toxin W5 and W30 residues and channel F813 residue (**Figure 3B, panel iv**). The overall shift of the toxin resulted in W24 no longer interacting with S2 residues.

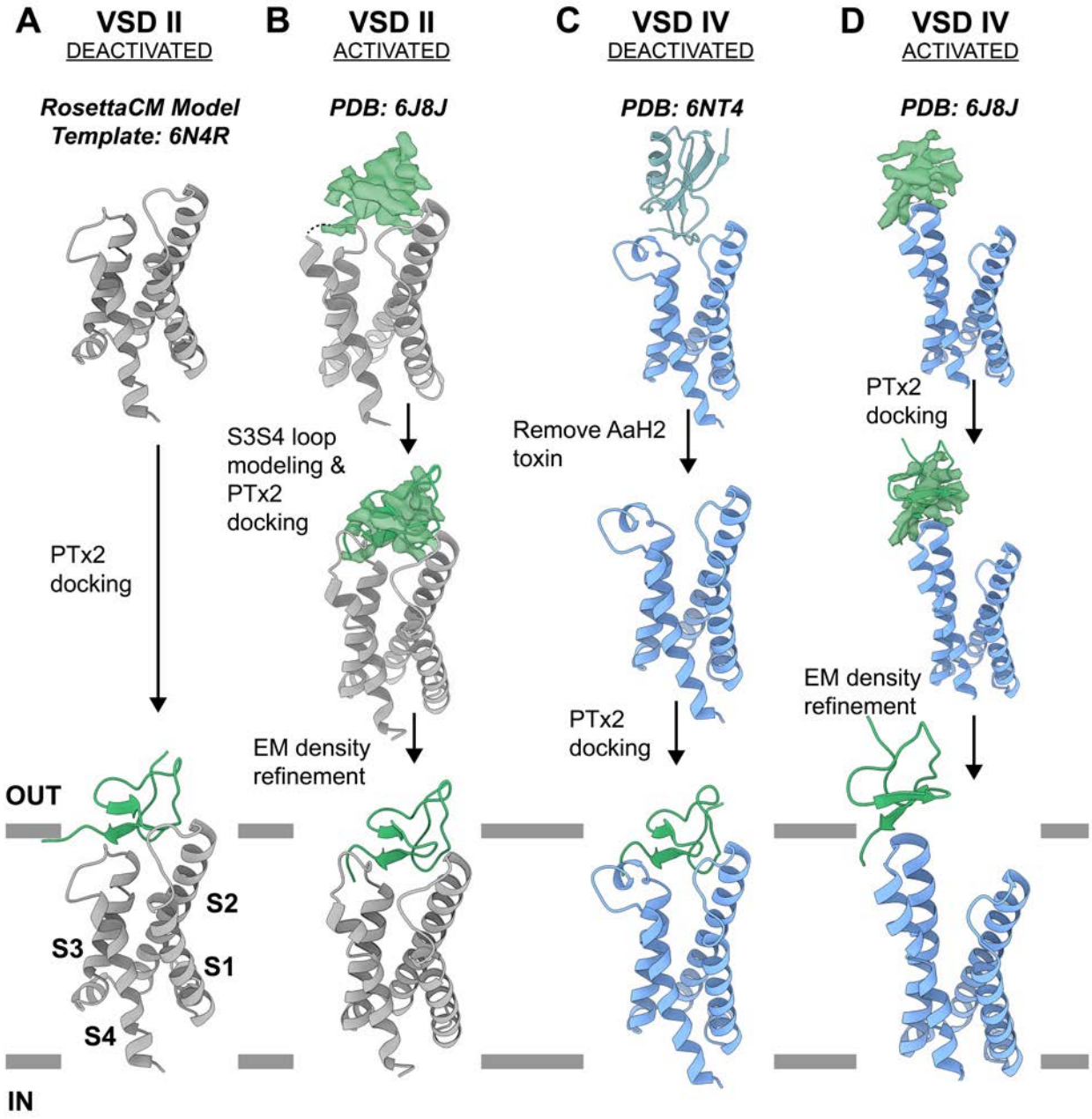

Figure 2. ***Workflow of the structural refinement, modeling, and docking process for different PTx2 – hNa$_V$1.7 VSD II and IV structures****. Solid gray lines denote the approximate positions of head groups of the lipid bilayers. "In" and "out" labels are added to represent intracellular and extracellular sides, respectively.*

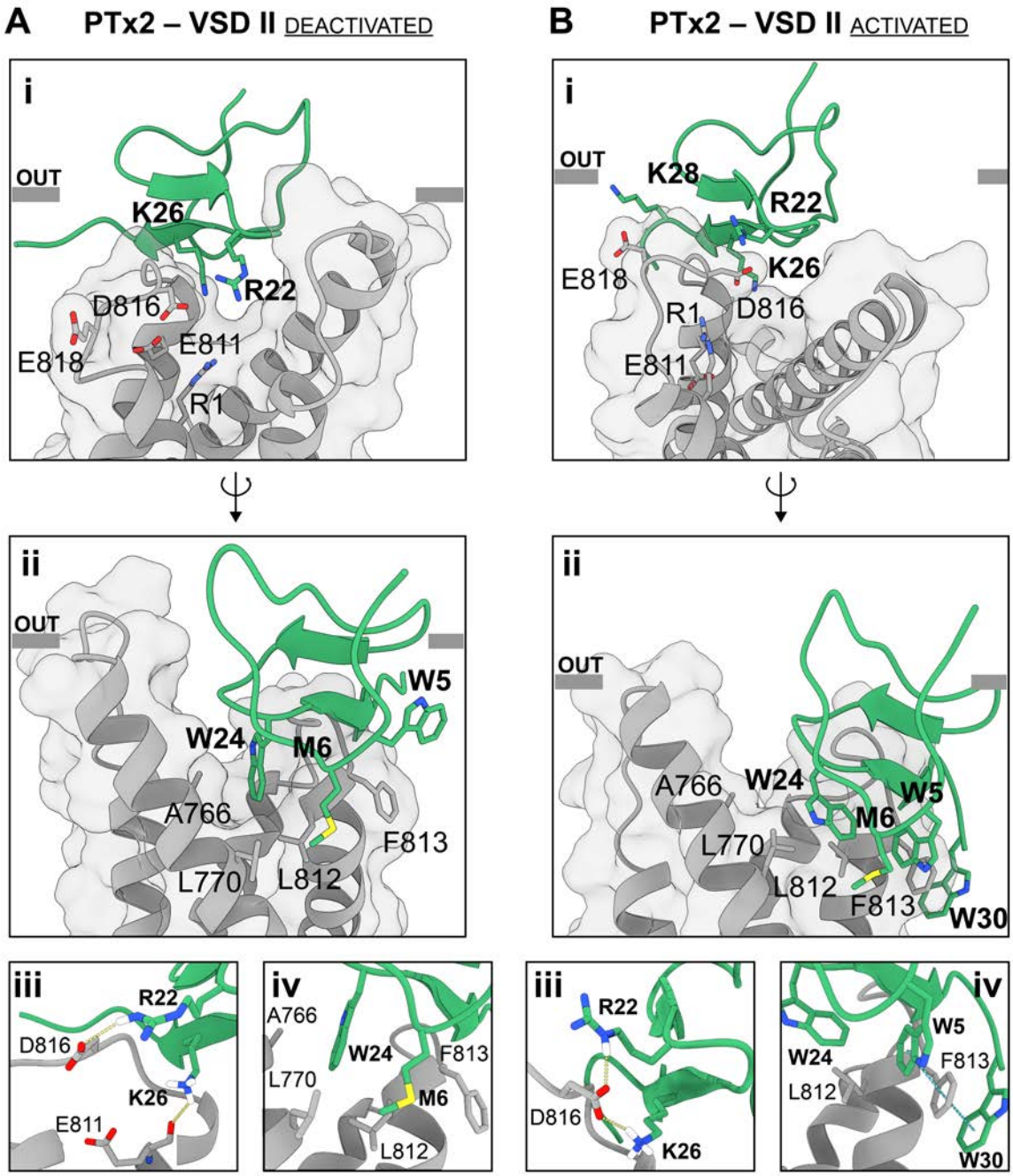

Figure 3. ***Structural models of PTx2 bound to hNa$_V$1.7 VSD II in the deactivated and activated states***. *Binding interface of PTx2 – deactivated VSD II (A) and PTx2 – activated VSD II (B) complexes of top scoring Rosetta models. i) Front view of interface highlighting interactions with the VSD that comprise the polar binding interface; "R1" highlights the position of the first gating charge. ii) Back view of the interface highlighting interactions with the VSD that comprise the hydrophobic or membrane-interacting interface. iii) detailed interactions at the polar interface; yellow dashed lines highlight hydrogen bonds. iv) detailed interactions at the hydrophobic interface; blue dashed lines highlight π - stacking interactions. The gray bar depicts the boundary of the outer leaflet of the cell membrane.*

Experimental results show that PTx2 can also bind to $Na_V1.7$ VSD IV and modulate channel inactivation[18], although with much lower potency (IC_{50} = 0.24 μM). Our models of PTx2 bound to both deactivated and activated VSD IV presented binding interfaces, which can also be separated into a polar interface and a hydrophobic interface. Our models revealed that the position and interface of PTx2 change significantly more between the deactivated and activated states of VSD IV compared to VSD II (**Supplementary Video 2**). Our model of PTx2 bound to the deactivated VSD IV was built using the experimental structure of the hNaV1.7 VSD IV in a deactivated state induced by binding of an α-scorpion toxin (PDB: 6NT4)[4], and it is important to note that the actual VSD IV deactivated state to which PTx2 binds may differ. In our final top Rosetta model, PTx2 is embedded in the membrane between the VSD IV S3 and S2 segments. hNav1.7 VSD IV residues D1586, E1589, and T1590 create an electronegative pocket that accommodates R22 and K26 from the toxin (**Figure 4A, panel i**). Toxin R22 extends into the VSD and establishes hydrogen bonds with channel D1586 while K26 interacts with G1586 at the top of the S3 segment (Figure 5A, panel iii). The hydrophobic interface is more complex in this case (**Figure 4A, panel ii**). PTx2 makes contact with residues in the VSD IV S2 segment, which are mainly hydrophobic interactions mediated by toxin residue W24 and channel residues Y1539 and W1538. Finally, toxin residues W5, M9, and W30, which also serve as membrane anchors, interact with several hydrophobic residues from the channel located in the S3 segment: M1582, F1583 and L1584 (Figure 5A, panel iv). In our models, a large conformational rearrangement of the VSD IV occurs between the deactivated and the activated state. As a result, the location of PTx2 also undergoes a dramatic change (**Supplementary Video 2**). In the activated state, the toxin is situated at the top of the S3 segment and does not establish interactions with the S2 segment. The polar interface observed in the activated VSD IV state (**Figure 4B, panel i**) is primarily mediated by the interaction between toxin residue K26 and channel residue E1589 (Figure 5B, panel iii), with PTx2 residue R22 not appearing to play a significant role in this interaction in contrast to the deactivated state. In the hydrophobic interface (**Figure 4B, panel ii**), the toxin uses its residues W5, M9, and W30 to anchor to the membrane and establish hydrophobic contacts with residues I1588, Y1591, F1592 from the channel (Figure 5B, panel iv). Notably, these hydrophobic channel's VSD IV residues are positioned far from the binding interface in the deactivated state. In contrast, the channel residues previously involved in the hydrophobic interface in the deactivated state (M1582, F1583 and L1584) now lie below the interface and do not interact with the toxin. (**Figure 4B, panel ii**).

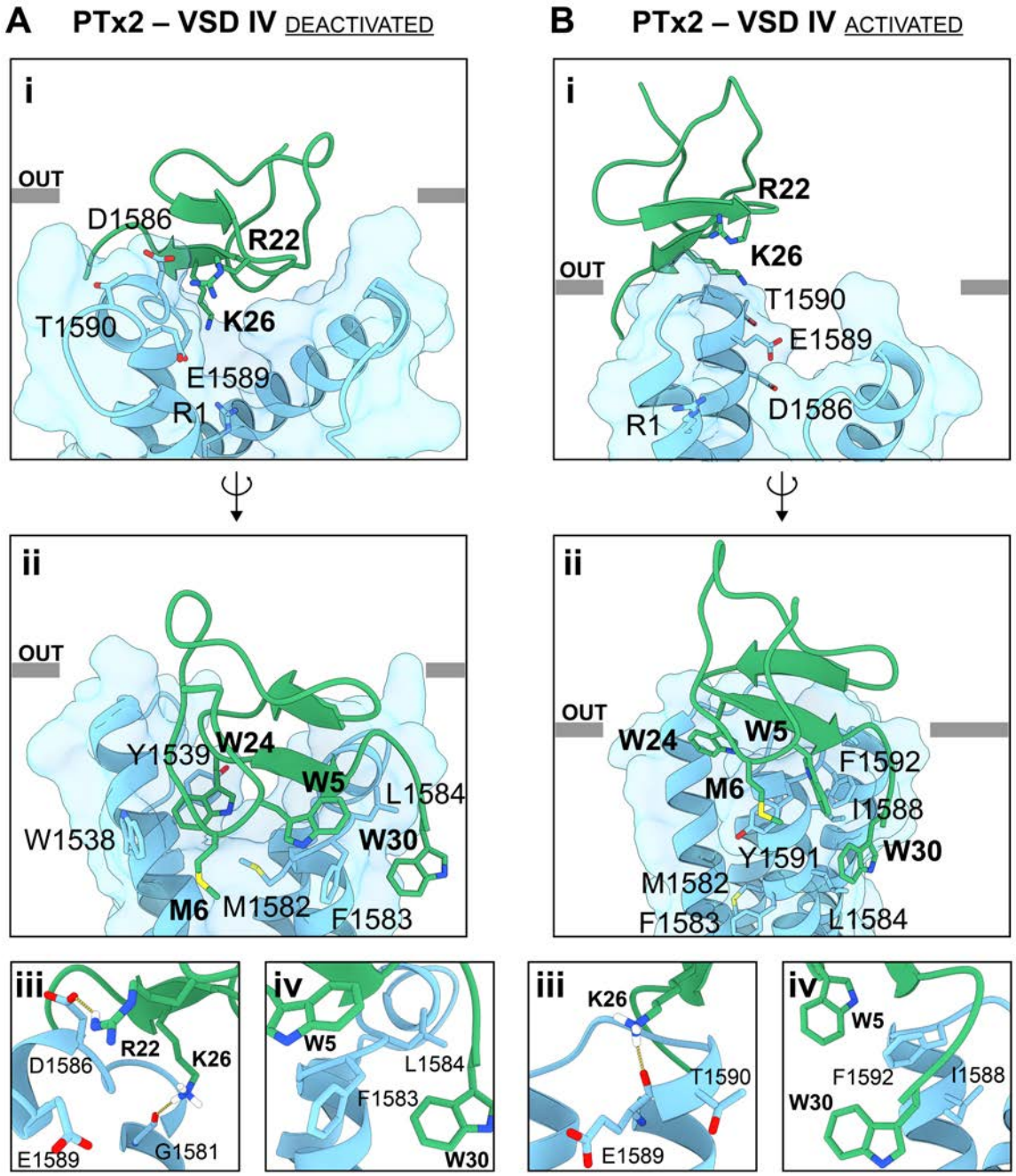

Figure 4. ***Structural models of PTx2 bound to hNa$_V$1.7 VSD IV in the deactivated and activated states***. *Binding interface of PTx2 – deactivated VSD IV (A) and PTx2 – activated VSD IV (B) complexes of top-scoring Rosetta models. i) Front view of the interface highlighting interactions with the VSD that comprise the polar binding interface; "R1" highlights the position of the first gating charge. ii) Back view of the interface highlighting interactions with the VSD that comprise the hydrophobic or membrane-interacting interface. iii) Detailed interactions at the polar interface; yellow dashed lines highlight hydrogen bonds. iv) Detailed interactions at the hydrophobic interface. The gray bar depicts the boundary of the outer leaflet of the cell membrane.*

2.2 Molecular dynamics simulations on PTx2 interactions with hNa$_V$1.7 VSD II and IV

Each PTx2 – hNa$_V$1.7 VSD complex was embedded into a POPC lipid membrane, then solvated with an aqueous 0.15 mM NaCl solution (example in **Figure 5**). Afterward, we performed molecular dynamics (MD) simulations on the docked structures to assess the stability of the docked models in a physiological environment, quantify the energetics of the binding process, and evaluate the effects of the lipids on the binding. For each PTx2 – hNa$_V$1.7 VSD complex simulation, the atomic coordinates over the whole simulation trajectory, excluding the equilibration process, were used to construct contact maps showing the residues involved in PTx2 – hNa$_V$1.7 VSD binding interactions in addition to the type and duration of the interactions (hydrophobic, hydrogen bond, salt bridges, π-π, or cation-π). In our analysis, a contact between two residues is considered significant and stable if it persists for more than 50% of the analyzed simulation time.

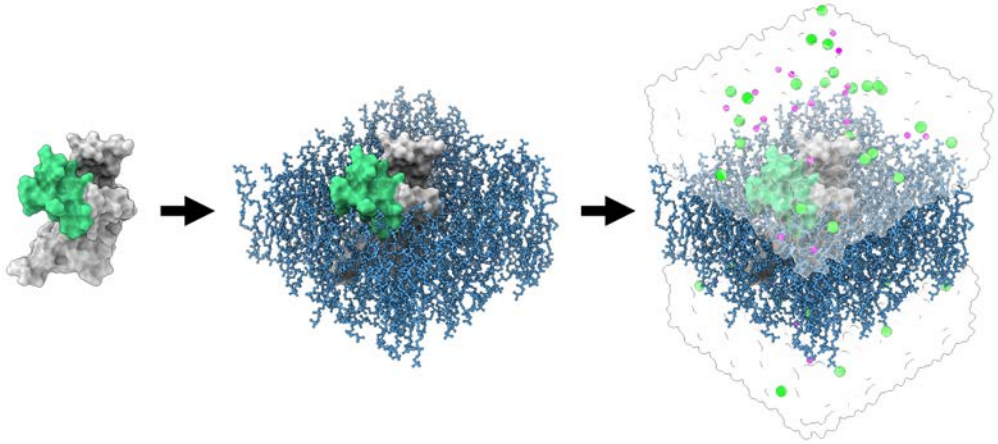

Figure 5*. **Creation process of a molecular system consisting of the PTx2 – hNa$_V$1.7 activated VSD II complex embedded in a POPC bilayer and solvated with** **aqueous** **0.15 M NaCl solution.** PTx2 and VSD II are shown as green and dark gray surfaces, respectively. The lipid membrane composed of POPC lipids are shown in blue sticks. Water is displayed as a transparent surface. Na^+ and Cl^- ions are displayed as purple and green spheres, respectively.*

PTx2 – hNa$_V$1.7 deactivated and activated VSD II. During the simulations, PTx2 remains bound to VSD II by wedging itself into a cleft between the S1-S2 and S3-S4 loops, as shown in **Figure 6A, D**. RMSD profiles in **Figure 6B, E** demonstrate that the toxin experienced only minor conformational changes during the simulations (~2.5 Å RMSD). On the other hand, the VSDs experienced more drastic conformational changes by the end of the simulations (~3.5 to 4.5 Å RMSD), likely due to the instability caused by their isolation from the rest of the channel.

The contact maps showing PTx2 interactions with VSD II in the deactivated and activated states are displayed in **Figure S1** and **Figure S3**, respectively. In both cases, the binding poses of PTx2 are very similar and are mediated predominantly by the formation of hydrogen bonds, hydrophobic interactions, and salt bridge formations with VSD II residues on the S3-S4 loop (L812, F813, L814, A815, D816), as shown in **Figure 7**. Throughout the simulation, PTx2 residues K26 and K27 formed significant (persisting for more than 50% of the analyzed simulation time) hydrogen bonds with VSD residues E811, F813, and A815. PTx2 residue R22 was observed to make a stable salt bridge with

VSD residue D816 for 78% of the simulation time. Hydrophobic contacts constituted most of the interactions between the toxin and VSD II (64-66%), followed by hydrogen bond formation (27-28%) (**Figure 6C, F**). PTx2 residues W5, V20, K26, K27, and L29 engaged in hydrogen bonding and hydrophobic interactions with VSD residues on the S3-S4 loop, while toxin residues L23 and W24 engaged in hydrophobic interactions with S1-S2 residues, forming two stable anchors to station the toxin in between the two loops.

Comparing PTx2 binding to VSD II in different states, PTx2 tends to form more hydrophobic interactions and salt bridges with VSD II in the deactivated state. In particular, the PTx2 – VSD II salt bridge pair R22-D816 only persisted for 52.7% of the simulation time in case of PTx2 binding to activated VSD II but persevered for up to 78% of the simulation time in the case of deactivated VSD II. In addition, the hydrophobic contact pairs W24-L770 (from S1-S2 loop) and V20-A815 (from S3-S4 loop) were seen for 49.5% and 68.1% of simulation time when the toxin binds to the activated VSD II but persisted for up to 75.8% and 81.3% of simulation time in the other case.

Consistent with our findings, an experimental scanning mutagenesis study has previously demonstrated that the LFLAD motif in the S3-S4 loop region is the main receptor site of PTx2 binding to VSD II.[23] In addition, our simulation showed that PTx2 residues L23 and W24 made stable hydrophobic contact with VSD II S2 residue I767 (**Figure 7C**). Indeed, the I767A mutant exhibited a 5-fold reduction in PTx2 potency[23] compared to the WT channel (IC_{50} changes from ~0.25 nM to ~1.25 nM), indicating such interactions to be important for the toxin to bind to the VSD.

Analysis of PTx2 interactions with POPC lipids when binding to VSD II in the deactivated and activated states were conducted and displayed in **Figure 8** (for contact maps, see **Figure S2** and **Figure S4**). PTx2 T8 formed sporadic hydrogen bonds with the surrounding lipids in both simulations. In the case of PTx2 binding to activated VSD II, more hydrophobic interactions (mainly by W5, W7, T8, W24, W30) and salt bridges formations (mainly by K4, K27) were observed compared to the deactivated VSD II simulation (only W5 and W24 engaged in substantial hydrophobic interactions, and no long-lasting salt bridges were built). For the deactivated VSD II simulation, however, PTx2 R13 and K27 participated in various π-π/cation-π interactions with lipids, which were absent in the other case.

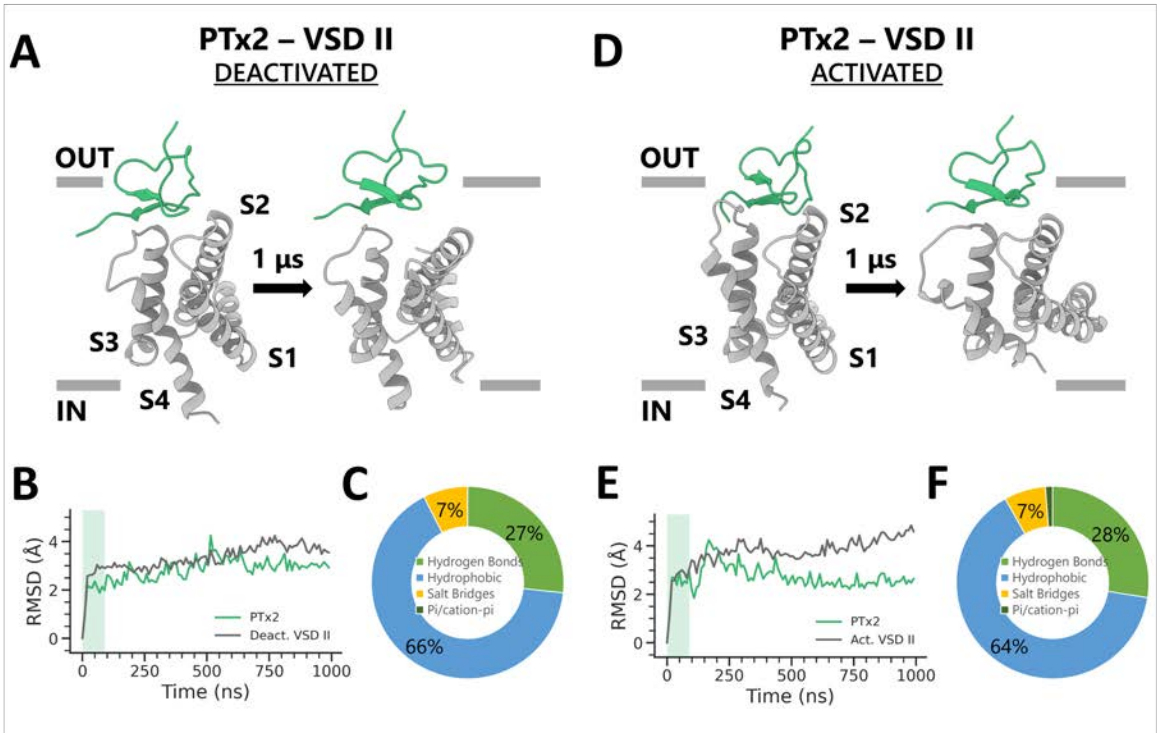

Figure 6. ***A general overview of the 1 µs molecular dynamics simulation of PTx2 – hNa$_V$1.7 VSD II in the deactivated (A, B, C) and activated states (D, E, F).*** *A, D) Conformational changes of the toxin – VSD complex after 1 µs long molecular dynamics simulation. B, E) Root-mean-square deviation (RMSD) time series of the backbone PTx2 and VSD atoms compared to the initial structures. The equilibration period is highlighted in green. C, F) Distribution of all toxin – VSD interaction types encountered during the simulation, computed by dividing the sum of a specific interaction type by the sum of all interactions across all simulation frames.*

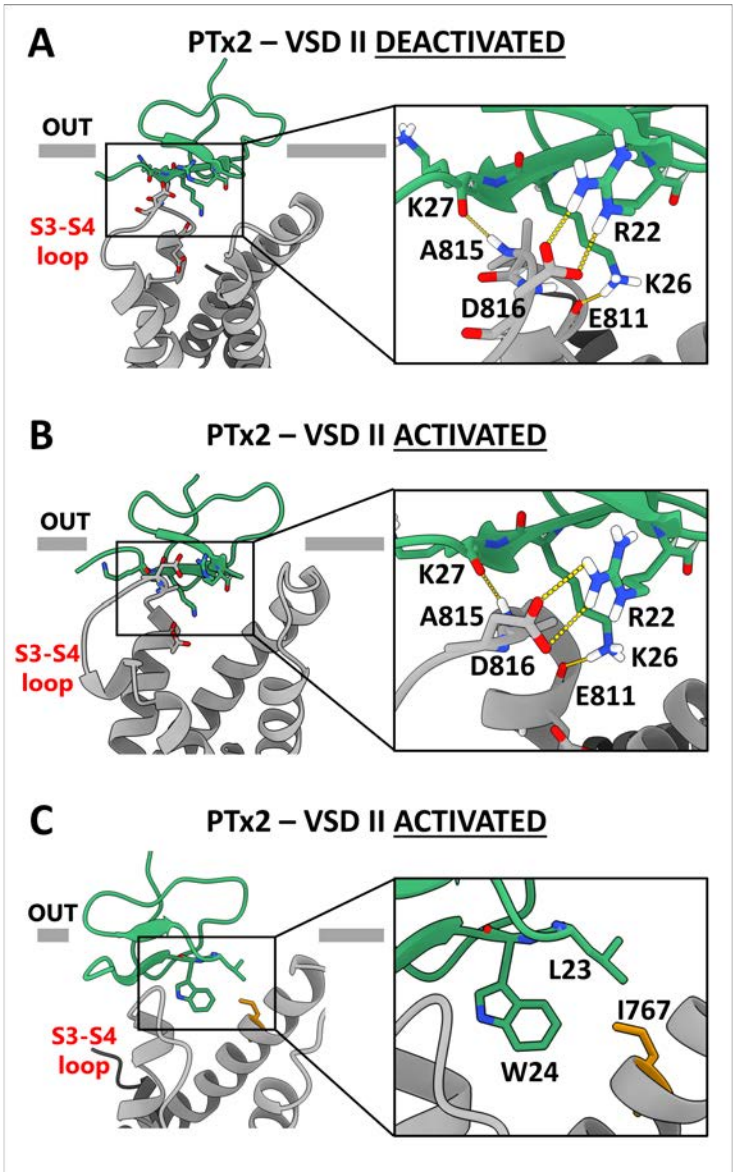

Figure 7. ***Specific interactions from molecular dynamics simulation of PTx2 – hNa$_V$1.7 VSD II in the deactivated (A) and activated states (B, C).*** *PTx2 is shown in green and the VSD is shown in gray. The gray bar depicts the boundary of the outer leaflet of the cell membrane. A) The salt bridge between D816 and R22 remains for most of the simulation. K26 makes a stable hydrogen bond with the backbone carbonyl of E811. B) R22 of PTx2 forms a stable salt bridge with D816 of the S3-S4 loop of VSD II. The sidechain of K26 from PTx2 forms a hydrogen bond with the backbone carbonyl of E811 at the top of the S4 helix of VSD II. C) W24 and L23 of PTx2 form stable hydrophobic contacts with VSD II, particularly with I767, serving as a hydrophobic anchor.*

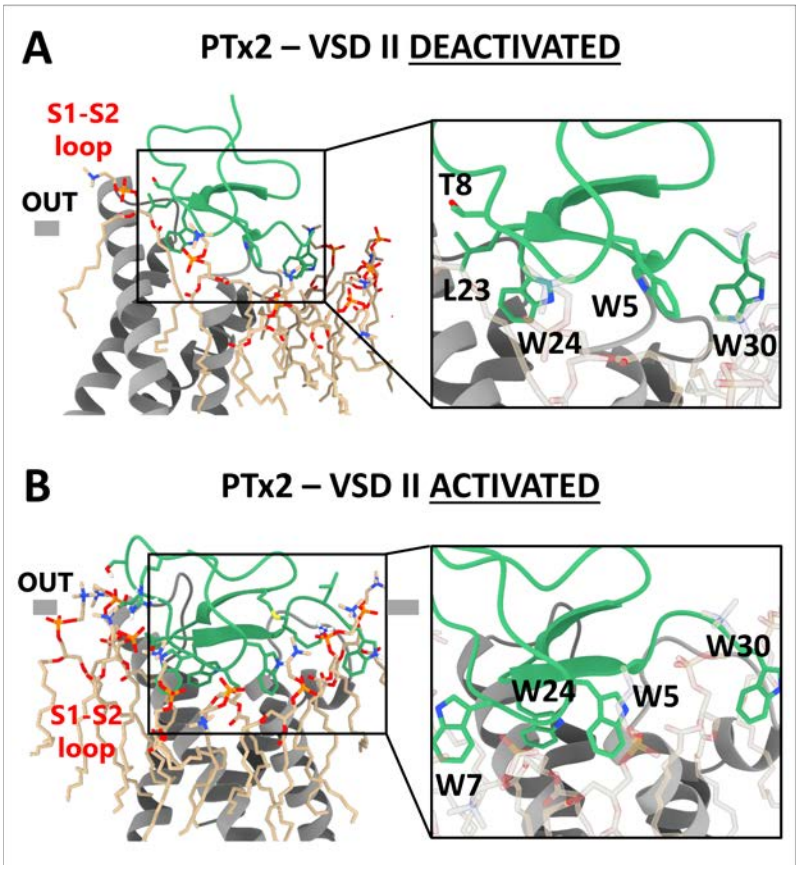

Figure 8. ***Lipid interactions from molecular dynamics simulation of PTx2 – hNa$_V$1.7 VSD II in the deactivated (A) and activated states (B).*** *PTx2 is shown in green and the VSD is shown in gray. Interactions are taken from the last frame of each simulation. A) In addition to hydrophobic contacts from tryptophan residues, L23 makes a hydrophobic contact with the membrane and T8 forms intermittent hydrogen bonds with the heads of POPC molecules. B) Four tryptophan residues make stable contacts with the membrane interface.*

PTx2 – hNa$_V$1.7 deactivated and activated VSD IV. Our simulations revealed that PTx2 binds to VSD IV differently depending on the latter's conformation. As shown in **Figure 9A**, the toxin binds to VSD IV in the deactivated conformation through a series of interactions with residues on the VSD S1-S2 and S3-S4 loops. During the simulation, PTx2 shifted its binding pose further into the binding pocket in between the S1-S2 and S3-S4 loops of VSD IV and experienced a slight deformation in the process, as indicated by the ~3 Å RMSD compared to the starting structure by the end of the simulation as seen in **Figure 9B**.

The contact maps showing PTx2 interactions with VSD IV in the deactivated and activated states are displayed in **Figure S5** and **Figure S7**, respectively. As shown in **Figure 9C**, hydrophobic contacts made up the majority of the interactions between PTx2 and the deactivated VSD IV (49%), followed by hydrogen bonds (35%) and salt bridges (11%). PTx2 residues L23 and W24 made significant hydrophobic contacts with VSD S1-S2 loop residues Y1537 (80.2% and 51.6% of simulation time, respectively). On the other hand, PTx2 residue V20 engaged in hydrophobic interactions with VSD IV residue A1585 on the S3-S4 loop for 70.3% of the simulation. PTx2 Lys triplet K26, K27, and K28

formed hydrogen bonds with VSD's residues G1581, F1583, A1585, and D1586 on the S3-S4 loop (60.4%, 93.4%, 100%, 64.8% of simulation time respectively, **Figure 10A, B**). On the opposite side of the binding interface, PTx2 residue T8 hydrogen bonded to VSD residue E1534 on the S1-S2 loop (**Figure 10A**). In sum, the hydrophobic and hydrogen bond anchors formed by PTx2 on both the S1-S2 and S3-S4 loops of VSD IV in the deactivated state helped secure the two edges of the toxin binding interface in the encounter complex.

Meanwhile, PTx2 binding to VSD IV in the activated conformation is localized to the S3-S4 loop, as seen in **Figure 9D**. As such, PTx2 experienced little changes to its conformation, evidenced by the ~2 Å RMSD compared to the starting structure by the end of the simulation as seen in **Figure 9E**. Unlike the binding to the deactivated state, hydrophobic interaction played a more dominant role in PTx2 binding to the activated VSD IV, followed by hydrogen bonds (61% and 39% of all interactions, respectively), with no salt bridges or π stacking interactions formed as displayed in **Figure 9F**. With the toxin perched atop of the S3-S4 loop, PTx2 residues K26 and K27 hydrogen bonded to VSD IV S3-S4 loop's E1589, Y1591, and V1593 (93.4%, 75.8%, and 84.6% of simulation time, visualized in **Figure 10C**). PTx2 residues W5, V20, and K27 also hydrophobically interacted with the same set of residues and with only sporadic contacts with neighboring residues.

Specific PTx2 residues that are involved in interactions with POPC lipids when binding to VSD IV in the deactivated and activated states are visualized in **Figure 11** and mapped in **Figure S6** and **Figure S8**. When binding to VSD IV in the deactivated state, PTx2 formed more salt bridges (mainly by K4, R13, K27, and K28) and π-π/cation-π interactions (primarily by W7) with the surrounding lipids. Conversely, when PTx2 was bound to the activated VSD IV, only K4 and K27 engaged in meaningful salt bridge formation and few π/cation-π contacts were observed with lipids. Nevertheless, T8 was observed to be involved in several hydrogen bonds that were not present in the prior case. In both simulations, W5, W7, W24, and W30 demonstrated substantial roles in terms of forming hydrophobic contacts with lipids.

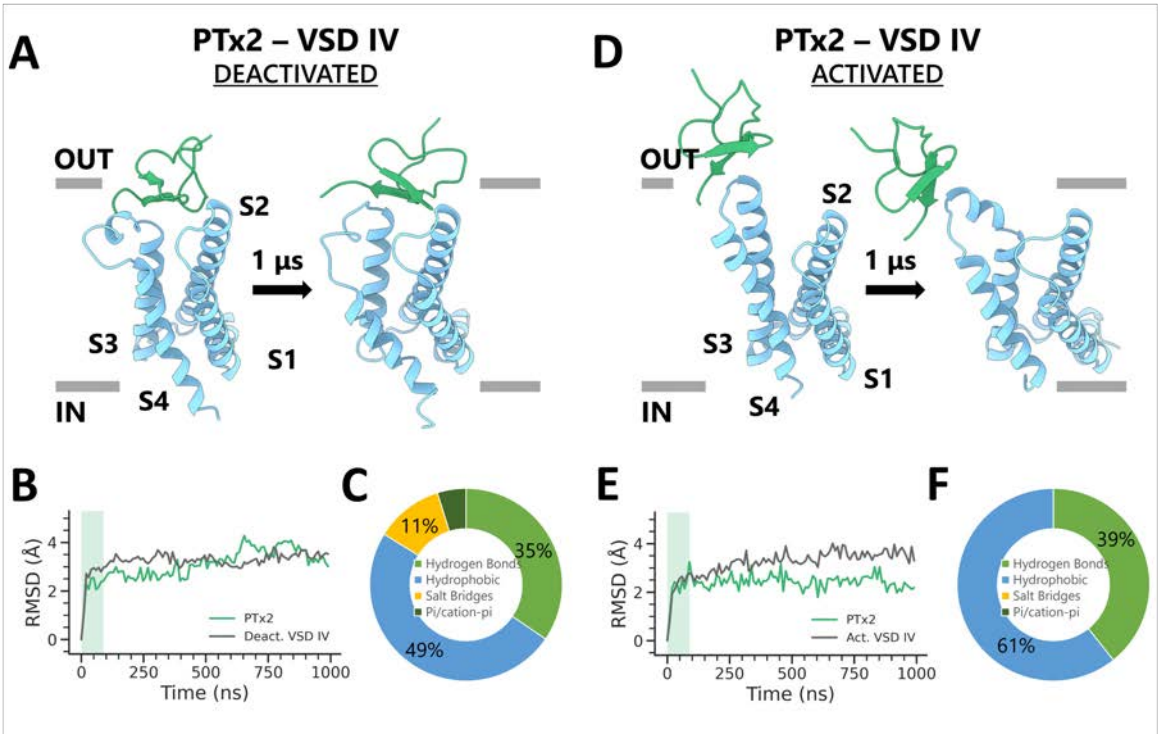

Figure 9. ***A general overview of the 1 µs molecular dynamics simulation of PTx2 – hNa$_V$1.7 VSD IV in the deactivated (A, B, C) and activated states (D, E, F).*** *A, D) Conformational changes of the PTx2 – VSD complex after 1 µs long molecular dynamics simulation. B, E) Root-mean-square deviation (RMSD) time series of the backbone PTx2 and VSD atoms compared to the initial structures. The equilibration period is highlighted in green. C, F) Distribution of all PTx2 – VSD interaction types encountered during the simulation, computed by dividing the sum of a specific interaction type by the sum of all interactions across all simulation frames.*

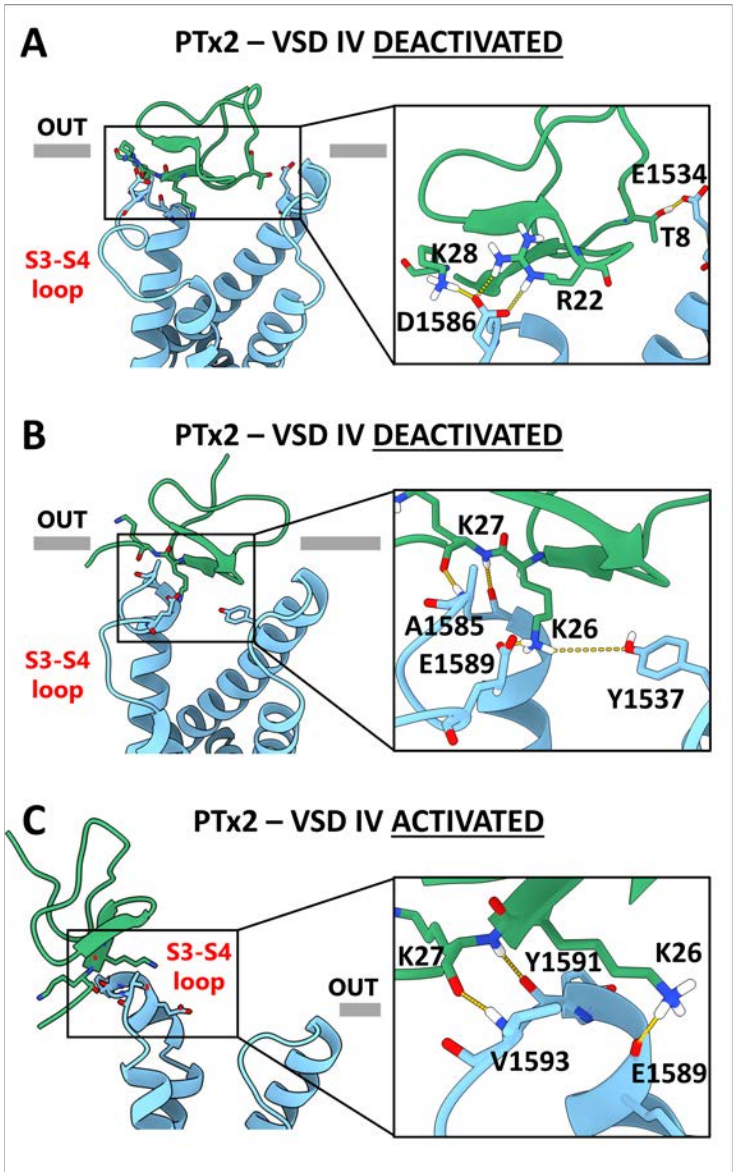

Figure 10. ***Specific interactions from molecular dynamics simulation of PTx2 – hNa$_V$1.7 VSD IV in the deactivated (A, B) and activated states (C).*** *PTx2 is shown in green and the VSD IV is shown in blue. The gray bar depicts the boundary of the outer leaflet of the cell membrane. A) Interactions with the deactivated VSD IV from the beginning of the simulation (following equilibration). The backbone of F1583 and A1585 participate in hydrogen bonds with the backbone of K27 of PTx2 while the D1586 side chain interacts with K28. One stable hydrogen bond interaction between E1534 on the top of the S1 helix and T8 of PTx2, but this breaks as the simulation progresses. B) PTx2 – VSD IV complex at the end of the simulation. The salt bridge with R22 and D1586 is now broken in favor of a new salt bridge between K26 and E1589. Y1537 from the S2 helix of VSD IV forms a weak hydrogen bond with K26. C) Interactions with the activated VSD IV. The backbone of V1593 and Y1591 of the S3-S4 loop interact with the backbone of K27 of PTx2. There are no interactions between PTx2 and the S1 helix or S1-S2 loop in activated state of VSD IV.*

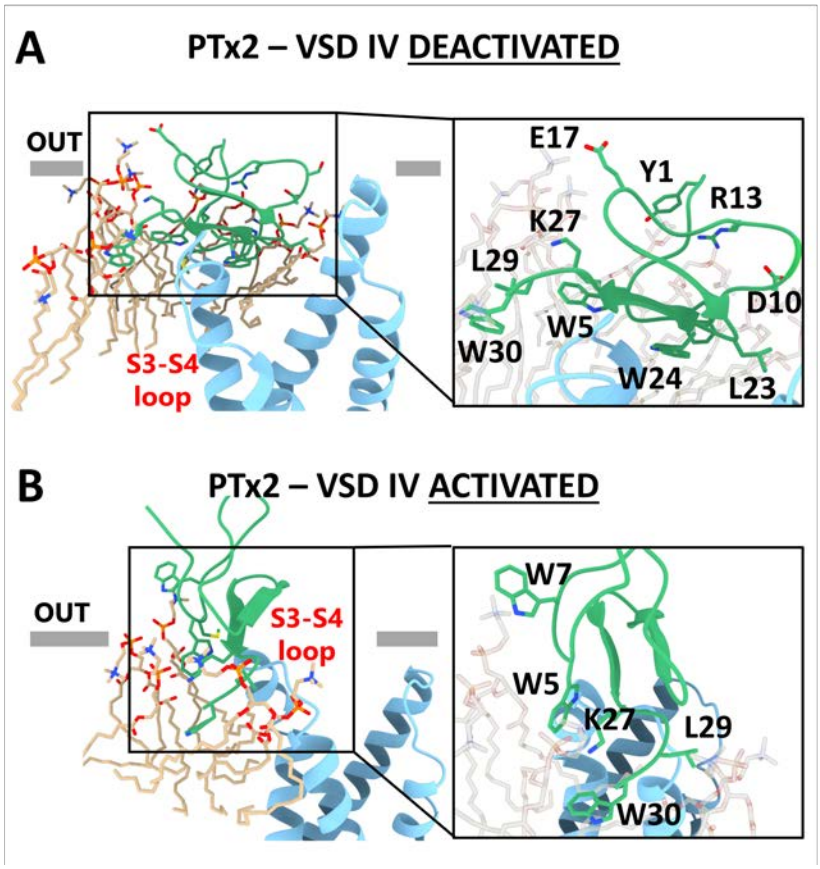

Figure 11. ***Lipid interactions from molecular dynamics simulation of PTx2 – hNa$_V$1.7 VSD IV in the deactivated (A) and activated states (B).*** *PTx2 is shown in green and the VSD IV is shown in blue. Interactions are taken from the last frame of each simulation. A) Due to its orientation with respect to the membrane, PTx2 makes considerably more contacts with lipid molecules in this simulation as compared to the activated state of VSD IV. In addition to hydrophobic contacts from tryptophan residues, L29, and L23, polar residues also make more hydrogen bonds with lipid headgroups. Namely, E17, K27, R13, and D10 all make hydrogen bonds and salt bridges with POPC lipids. B) Three tryptophan residues as well as L29 make stable hydrophobic contacts with the membrane interface while K27 hydrogen bonds with lipid head groups.*

3.3 Analysis of binding energetics

Using our all-atom MD simulation trajectories, we employed the implicit-solvent MM/PBSA methodology[48] to calculate the binding affinities of PTx2 to different states of hNa$_V$1.7 VSD II and IV. **Figure 12** shows the time series of PTx2 – VSD binding enthalpies of the systems estimated using MM/PBSA. Overall, there were brief periods of large energy fluctuations, but the overall trends of each system remain relatively stable. The deactivated states of both VSD II and IV exhibited more favorable binding enthalpies compared to the activated states throughout the simulations. As shown in **Table 1**, the average enthalpies were calculated using block averages taken from the last 200 ns of the simulation to exclude periods of large energy fluctuations before 800 ns as shown in **Figure**

12. The optimal block sizes for the systems were selected to minimize the standard errors of the results. Our results indicate that PTx2 binding to the deactivated VSD II was found to be the most favorable out of all states, followed by deactivated VSD IV, activated VSD II, and finally, activated VSD IV (computed ΔG_{bind} of -23.3 ± 4.4, -13.5 ± 4.0, 8.8 ± 2.9, and 9.5 ± 1.8 kcal/mol, respectively).

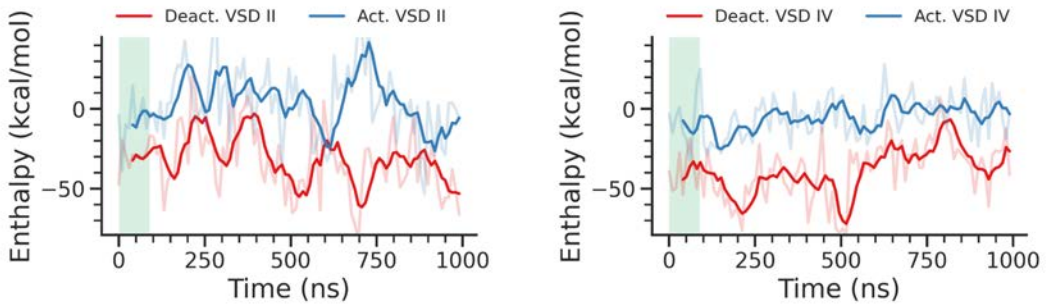

Figure 12. ***Time series of binding enthalpy of the PTx2 – hNa$_V$1.7 VSD II and IV complexes during MD simulations.*** *50-ns rolling averages are plotted on top of the raw data to better display the trends. The equilibration period is highlighted in green.*

Consistent with our findings that PTx2 binds better to the deactivated state of the VSDs, electrophysiology experiments previously revealed that PTx2 antagonizes Na$_V$1.7 at ~60-fold lower potency when the membrane potential is held at a voltage that promotes VSD activation[23]. In addition, another study indicated that the estimated IC$_{50}$ for PTx2 inhibition of Na$_V$1.7 activation (i.e., binding to deactivated VSD II) is ~400-fold lower than the apparent IC$_{50}$ for the inhibition of inactivation (i.e., binding to deactivated VSD IV)[18], and thus agrees with our findings that PTx2 binds most favorably to the deactivated VSD II.

Table 1. ***MM/PBSA binding energies in PTx2 – hNa$_V$1.7 VSD systems computed from the last 200 ns of the all-atom molecular dynamics simulations.***

Systems	Calculation block window (ns)	$\Delta H_{MM/PBSA}$ (kcal/mol)	-TΔS (kcal/mol)	ΔG_{bind} (kcal/mol)
PTx2 – Deactivated VSD II	51	-41.5 ± 3.7	18.3 ± 2.4	-23.3 ± 4.4
PTx2 – Activated VSD II	41	-12.0 ± 2.5	20.8 ± 1.3	8.8 ± 2.9
PTx2 – Deactivated VSD IV	63	-34.3 ± 3.4	20.8 ± 2.2	-13.5 ± 4.0
PTx2 – Activated VSD IV	55	-2.1 ± 1.3	11.5 ± 1.2	9.5 ± 1.8

In **Figure 13**, we utilized the implicit-solvent MM/GBSA methodology[52] to estimate the binding free energy contributions of individual residues to quantify the energetic disparities in PTx2 binding to VSD II and IV on a per-residue basis (for a more extensive list of per-residue binding free energies computed using MM/GBSA, see **Figure S9Error! Reference source not found.**). Although less t heoretically rigorous[55,56], MM/GBSA[52] was used instead of MM/PBSA[48] for per-residue energy analysis as the non-polar solvation energies are not decomposable with Poisson-Boltzmann implicit solvent model associated with MM/PBSA, and hence such energies are not counted toward the binding free energy of each residue (for MM/PBSA binding free energy results, see **Figure S10**). The

energy values obtained are rough estimates as neither implicit nor explicit membrane was incorporated in the calculations.

In **Figure 13A**, we show the top 10 PTx2 residues with the greatest free energy of binding with different states of the VSD. From an energetic perspective, PTx2 residues R22, L23, W24, and K27 are the main contributors to PTx2 – VSD II and IV binding through the formation of hydrogen bonds, hydrophobic interactions, and salt bridges. The most apparent difference is observed in the case of toxin binding to the activated state of the VSD IV. Although PTx2 residue R22 and L23 play dominant roles in binding to both states of the VSD II and the deactivated state of VSD IV, they fail to form any significant interactions when binding to the activated state of the VSD IV as the bound toxin's orientation places the residues far from potential binding partners (**Figure 4B**). PTx2 residue K28 is another special case, in which it has the most favorable binding free energy when binding to the deactivated VSD IV but less so with the other states. This observation can be attributed to the fact that K28 formed a stable hydrogen bond with D1586 (64.8% of simulation time) only when binding to VSD IV in the deactivated state (**Figure S5**).

Figure 13A shows PTx2 residues tend to bind more favorably to the VSD II in a deactivated state compared to an activated state. Interestingly, **Figure 13B**, which illustrates the binding free energies of notable VSD II residues that bind with PTx2, shows little difference between the activated and deactivated states from the perspective of VSD II residues. PTx2 also makes additional contacts with the lipid membrane when binding to VSD II in deactivated state as compared to the activated state () which may explain the overall more favorable binding of PTx2 to the deactivated state of VSD II. Moreover, **Figure 13C**, which shows the binding free energies of notable VSD IV residues that bind with PTx2, displays a clear difference in PTx2 binding when it binds to the activated compared to the deactivated state. In other words, PTx2 makes more favorable protein-protein contacts with the deactivated VSD IV as compared to the activated VSD IV.

When PTx2 binds to VSD IV in the deactivated state, it engages in hydrophobic interactions with S2 helix Y1537, S3 helix F1583, and S3-S4 loop L1584 (**Figure S5**). In addition, it also forms hydrogen bonds with S3 helix G1581 and S3-S4 loop A1585, D1586, and E1589. However, when the toxin binds to VSD IV in the activated state, it creates hydrogen bonds with residues closer to the middle of the S3-S4 loop like E1589, Y1591, and V1593 and forms hydrophobic interaction with F1592 (**Figure S7Error! Reference source not found.**). These differences in PTx2 – hNa_V1.7 VSD IV interactions a re due to PTx2 binding deeper (with respect to its position in the membrane) to VSD IV in the deactivated state (**Figure 4A**). In contrast, PTx2 binds shallower with VSD IV while the latter is in the activated state, and consequently only VSD residues at the top of the S3-S4 loop became involved in the binding process (**Figure 4B**). PTx2 also makes substantially fewer interactions with the lipid membrane when binding to the VSD IV in an activated state compared to a deactivated state (visualized in **Figure 11** and by comparing the contact map in **Figure S8** vs. **Figure S6**).

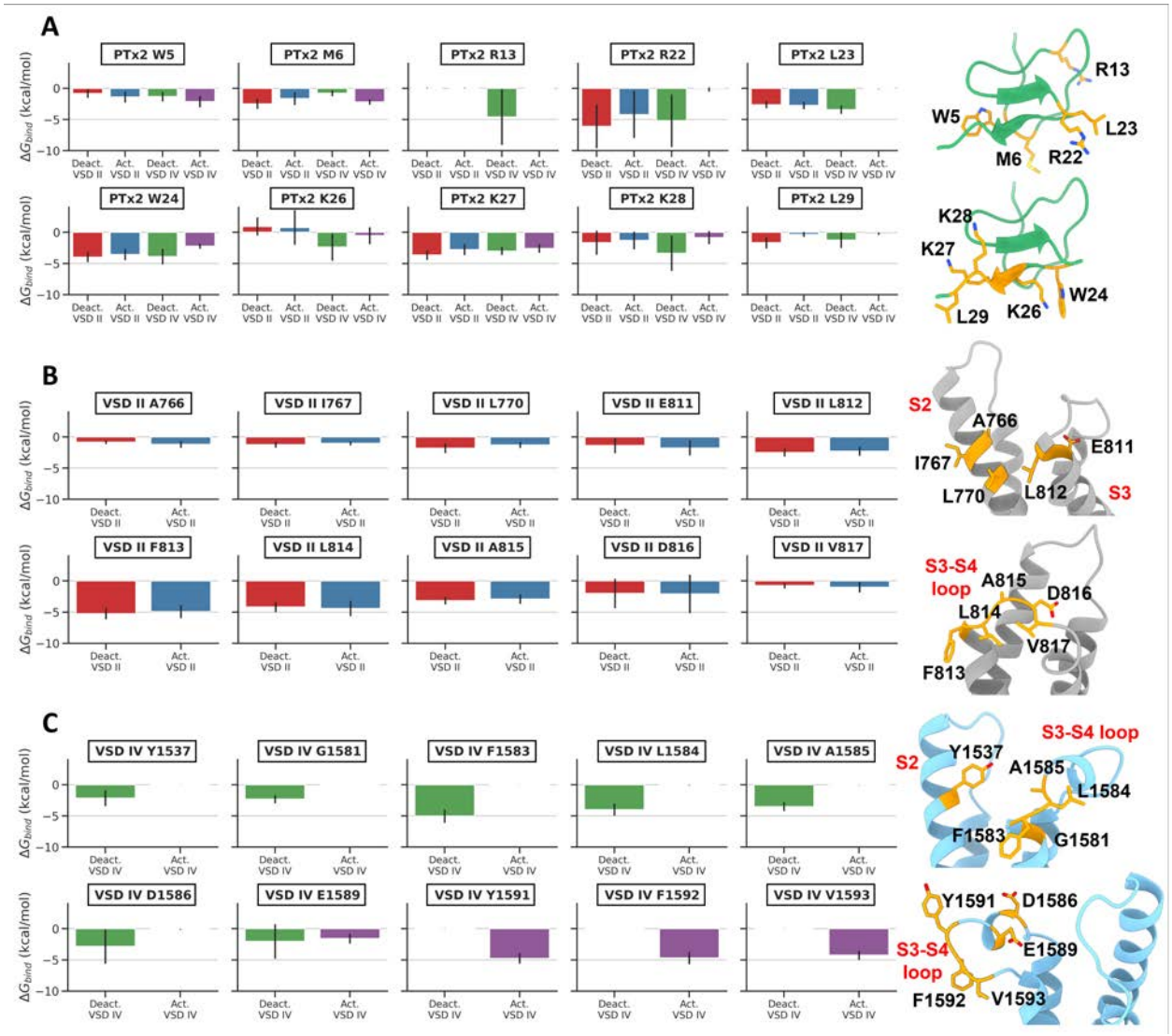

Figure 13. ***MM/GBSA binding energetic contribution of each residue toward the binding process for different PTx2 – hNa$_V$1.7 VSD systems.*** *Residues named on each row are visualized in orange to the right of the plots. A) Binding free energies exerted by top 10 most dominant PTx2 residues (ranked by combined free energies) when interacting with VSD II and IV in different states. B) Binding free energies exerted by top 10 most dominant VSD II residues in different states when binding with PTx2. C) Binding free energies exerted by top 10 most dominant VSD IV residues in different states when binding with PTx2.*

A strategy to improve PTx2's inhibition of hNa$_V$1.7 is to optimize its interactions with the lipids of the cell membrane. Experimental studies have revealed that the binding of PTx2 to the lipid membrane is a major factor in its potency as an inhibitor of hNa$_V$1.7[26]. As our MM/GBSA binding free energy calculations did not account for the lipid membrane, we performed AMBER linear interaction energy analysis[39,53] on our all-atom MD simulations to compute the electrostatic and van der Waals interaction energies of PTx2 with explicit POPC lipids and VSD II/IV, as shown in **Figure 14** (for the full analysis with more residues, see **Figure S11**). The AMBER energy estimates, although are less

rigorous and comprehensive than the previous analysis with MM/GBSA, can provide a foundation for more detailed research into protein-lipid interactions.

In **Figure 14**, PTx2 residues K4, W5, M6, W7, and T8, which form the main lipid interaction surface, and R22, W24, K26, K27, K28, and W30 that also contributed to lipid binding (as demonstrated in earlier contact analysis and visualized in **Figure 8** and **Figure 11**) all display favorable binding interaction energy with POPC and VSD II/IV. In particular, the four tryptophan residues of PTx2 (W5, W7, W24 and W30) play a key role in anchoring PTx2 to the cell membrane. Tight binding of PTx2 to the outer leaflet of the cell membrane seems to be critical for the inhibition of PTx2 on $hNa_V1.7$ channels[26]. Consistent with our findings, available mutagenesis studies that produced W5Y, W7Y, W24Y, and W30Y led to 6- to 291-fold reduction in potency in the inhibition of $hNa_V1.7$[26], indicating the importance of these residues for PTx2 binding to $hNa_V1.7$ (the mutation to Tyr was done since Tyr is more polar than Trp and is less suited to bind at the phospholipid interface[57]).

Interestingly, K4 and W7 exhibit significantly more favorable interaction energies when binding to activated VSD II and deactivated VSD IV, but less so with deactivated VSD II and activated VSD IV. The latter two states are of special importance to pain therapy via channel inhibition, as stabilizing VSD II in the deactivated state can prevent $hNa_V1.7$ channel opening and stabilizing VSD IV in the activated state can keep the channel in an inactivated, non-conducting state. Our results suggest that mutations of these residues may be promising in order to increase the affinity of the toxin for either deactivated VSD II or activated VSD IV. On the same note, W5, T8, R13, R22, L23, and W24 might also be good mutation candidates if the goal is to stabilize VSD IV activation as these residues have remarkably less binding interaction energy with this state compared to other states.

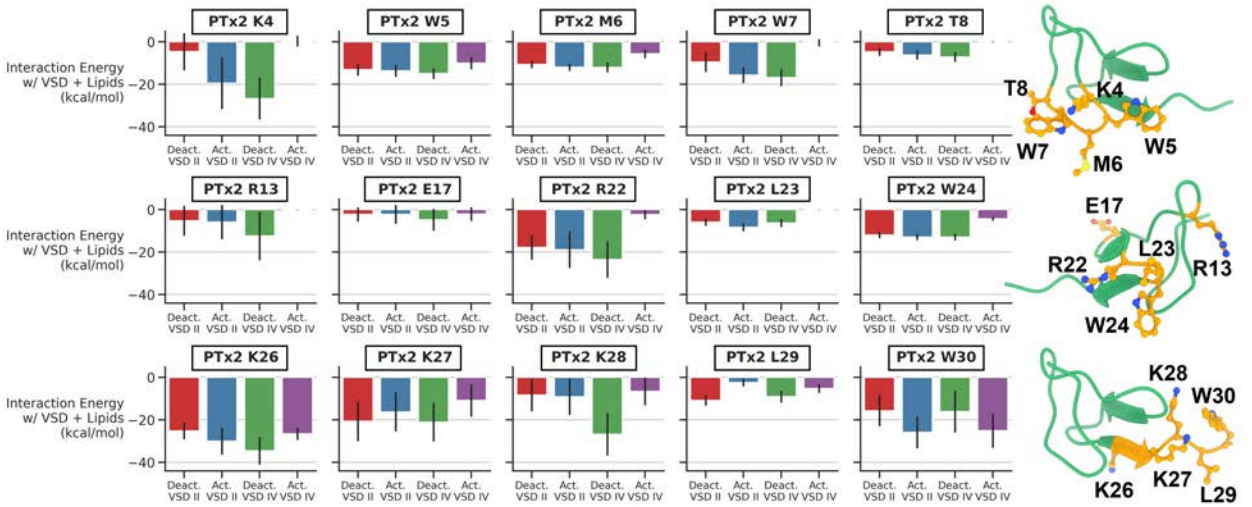

Figure 14. ***AMBER interaction energies (van der Waals + electrostatic) contributed by each PTx2 residue toward the binding process for different systems.*** *Residues named on each row are visualized in orange to the right of the plots. Only PTx2 residues with combined energy magnitude across all systems greater than 10 kcal/mol when interacting with each VSD system and the surrounding lipids are displayed.*

3. Discussion

In this study, we combined structural modeling, docking, and molecular dynamics simulations to capture the binding mechanisms and relative energies by which PTx2 can modulate $hNa_V1.7$ channel gating by binding to VSD II and IV. Our computational strategy successfully reproduces the binding locations of PTx2 to $hNa_V1.7$ VSD II & IV in the activated state as captured in experiments[23]. We further expanded the approach to analyze PTx2 binding to VSD II & IV in the deactivated state. In agreement with experimental mutagenesis studies[23,26], our findings demonstrated that PTx2 binds to VSD II mainly through hydrogen bonding and hydrophobic interactions with the LFLAD motif in the S3-S4 loop region. In addition, PTx2 made numerous stable hydrophobic contacts with VSD II residues on the S1-S2 loop regardless of whether the VSD is in the deactivated or activated state. Interestingly, the toxin formed more and longer-lasting hydrophobic interactions with VSD II residues when the latter is in the deactivated state, which might be one of the reasons why the toxin has a higher binding affinity for this state[18].

The lower affinity binding of PTx2 to the VSD IV is very different depending on which state the latter is in. PTx2 binding to deactivated VSD IV consists of the formation of stable hydrophobic interactions, hydrogen bonds, and salt bridges with residues on both S1-S2 and S3-S4 loops. However, PTx2 binding to activated VSD IV is localized strictly to residues on the S3-S4 loops. Our analysis of the binding energetics of PTx2 to different states of VSD II and IV demonstrated remarkable agreement with experimental results[23]: PTx2 binds better to the deactivated states of VSD II and IV, but significantly stronger to VSD II.

Here, we demonstrated that using computational modeling and simulation tools, we can accurately model the atomic-resolution structures and relative energetics of peptide toxin interactions with $hNa_V1.7$ in different conformational states. This allows for the accurate prediction of key binding interactions and design of more potent and selective peptides targeting $hNa_V1.7$ or other ion channels. Additionally, computational approaches can analyze large data sets quickly and accurately, allowing for the rapid identification of peptide-ion channel interactions responsible for conformational state and channel subtype specificities. In our study, we only modeled and simulated the VSDs of the channel to reduce computational cost, which could lead to undesirable instability during the simulations. In the future, we could expand our study by simulating for longer periods of time with multiple replicas and including full-channel structural models. Moreover, our methodology can be expanded to simulate the effects of various environmental conditions on peptide-ion channel interactions, such as varied membrane lipid composition other than pure POPC, pH, temperature, and ionic concentrations. Doing so will allow researchers to obtain a better understanding of how peptide-ion channel interactions are affected by different environmental conditions and can help inform experimental design.

Although the computational workflow in our study can provide valuable insights into the complexities of ligand-docking at atomic resolution, several drawbacks are associated with each methodology. Peptide backbone flexibility, especially at the N- and C- termini, is difficult to capture during the protein-protein docking and, therefore, RosettaDock might not be able to sample the full range of possible toxin conformations. Additionally, Rosetta scoring uses an implicit membrane model that might not account for energetic contributions involving membrane lipids that could be

important to stabilize the toxin pose. Although lipid membrane can be explicitly included in MD simulations, simulation accuracy often depends on the quality of the force field and parameters used in the simulation, and it can be difficult to determine the best set of parameters for any given system[58]. Fully atomistic molecular dynamics simulations are limited by their timescale (ns to μs), and hence advanced simulation techniques need to be employed to observe large-scale protein conformational transitions[59,60]. For estimating the free energy of binding, MM/PBSA methodology may suffer from accuracy problems especially for predicting absolute binding free energies as was demonstrated by a study done by *Sheng et al.*[61] The accuracy can be improved such as by damping the solvated and Coulombic terms for highly charged systems[61,62], using residue type-specific dielectric constants[63], and applying potentially more accurate entropy calculation methods[56]. Although less theoretically rigorous than MM/PBSA, MM/GBSA methodology have been shown to perform better than MM/PBSA in ranking the binding affinities of ligands for many systems, especially those without metal ions in the binding sites[55]. However, the lack of support for implicit membrane can be problematic in assessing ligand binding that involves significant lipid interactions. These and other molecular simulation methodology advancements will be explored in the follow-up studies with the current work providing a necessary framework and achieving a good agreement with several experimental findings[18,23].

In conclusion, our molecular modeling and simulation protocol can be a helpful guide for designing more potent therapeutic peptide variants with improved selectivity for different states of the channel as well as other Na_V channel subtypes as will be explored in follow-up studies. In addition, our results demonstrate that the interactions between PTx2 residues and lipids are important for state-specific binding to $Na_V1.7$ VSDs and should be considered in future channel inhibitor studies. These findings open the possibility to improve the balance of VSD and lipid-binding capability of the toxin and, consequently, its efficacy as a channel inhibitor. We anticipate that this methodology can also be expanded to study the interactions between other peptides and ion channels. Advancing our understanding of the molecular mechanisms of ion channel modulation by peptide toxins will allow us to harness the full potential of these molecules for therapeutical applications.

4. Acknowledgments

We would like to thank all members of the I.V., C.E.C. and V.Y.-Y. laboratories for helpful discussions. This work was supported by National Institutes of Health Common Fund Grant OT2OD026580 (to C.E.C. and I.V.), National Heart, Lung, and Blood Institute (NHLBI) grants R01HL128537, R01HL152681, and U01HL126273 (to C.E.C., V.Y.-Y. and I.V.), American Heart Association Career Development Award grant 19CDA34770101 (to I.V.), National Science Foundation travel grant 2032486 (to I.V.), UC Davis Department of Physiology and Membrane Biology Research Partnership Fund (to C.E.C. and I.V.) as well as UC Davis T32 Predoctoral Training in Basic and Translational Cardiovascular Medicine fellowship supported in part by NHLBI Institutional Training Grant T32HL086350 (to K.N.) and UC Davis Chemical Biology Program fellowship supported in part by National Institute of General Medical Sciences (NIGMS) Institutional Training Grant 5T32GM136597-02 (to K.C.R.). Computer allocations were provided through Extreme Science and Engineering Discovery Environment (XSEDE) grant MCB170095 (to I.V., C.E.C., and V.Y.-Y.), Texas Advanced Computing Center (TACC) Leadership Resource and Pathways Allocations MCB20010 (I.V., C.E.C., and V.Y.-Y.), Oracle cloud credits award (to I.V., C.E.C.), Pittsburgh Supercomputing Center (PSC) Anton 2 allocations PSCA17085P, MCB160089P, PSCA18077P, PSCA17085P, PSCA16108P (to I.V., C.E.C., and

V.Y.-Y.). Anton 2 computer time was provided by the Pittsburgh Supercomputing Center (PSC) through Grant R01GM116961 from the National Institutes of Health. The Anton 2 machine at PSC was generously made available by D.E. Shaw Research.

5. References

1. Ahern, C. A., Payandeh, J., Bosmans, F. & Chanda, B. The hitchhiker's guide to the voltage-gated sodium channel galaxy. *J. Gen. Physiol.* **147**, 1–24 (2016).
2. Bennett, D. L., Clark, A. J., Huang, J., Waxman, S. G. & Dib-Hajj, S. D. The Role of Voltage-Gated Sodium Channels in Pain Signaling. *Physiol. Rev.* **99**, 1079–1151 (2019).
3. Capes, D. L., Goldschen-Ohm, M. P., Arcisio-Miranda, M., Bezanilla, F. & Chanda, B. Domain IV voltage-sensor movement is both sufficient and rate limiting for fast inactivation in sodium channels. *J. Gen. Physiol.* **142**, 101–112 (2013).
4. Clairfeuille, T. *et al.* Structural basis of α-scorpion toxin action on Nav channels. *Science* **363**, (2019).
5. Chanda, B., Asamoah, O. K. & Bezanilla, F. Coupling interactions between voltage sensors of the sodium channel as revealed by site-specific measurements. *J. Gen. Physiol.* **123**, 217–230 (2004).
6. Chanda, B. & Bezanilla, F. Tracking voltage-dependent conformational changes in skeletal muscle sodium channel during activation. *J. Gen. Physiol.* **120**, 629–645 (2002).
7. Chowdhury, S. & Chanda, B. Sodium channels caught in the act. *Science* **363**, 1278–1279 (2019).
8. Nassar, M. A. *et al.* Nociceptor-specific gene deletion reveals a major role for Nav1.7 (PN1) in acute and inflammatory pain. *Proc. Natl. Acad. Sci.* **101**, 12706–12711 (2004).
9. Golshani, A. E., Kamdar, A. A., Spence, S. C. & Beckmann, N. M. Congenital Indifference to Pain: An Illustrated Case Report and Literature Review. *J. Radiol. Case Rep.* **8**, 16–23 (2014).
10. Dib-Hajj, S. D., Yang, Y., Black, J. A. & Waxman, S. G. The NaV1.7 sodium channel: from molecule to man. *Nat. Rev. Neurosci.* **14**, 49–62 (2013).
11. Yang, X., Wei, X., Mu, Y., Li, Q. & Liu, J. A review of the mechanism of the central analgesic effect of lidocaine. *Medicine (Baltimore)* **99**, e19898 (2020).
12. Hsu, E. S. Medication Overuse in Chronic Pain. *Curr. Pain Headache Rep.* **21**, 2 (2017).
13. Nguyen, P. T. *et al.* Computational design of peptides to target NaV1.7 channel with high potency and selectivity for the treatment of pain. *eLife* **11**, e81727 (2022).
14. Nguyen, P. T. & Yarov-Yarovoy, V. Towards Structure-Guided Development of Pain Therapeutics Targeting Voltage-Gated Sodium Channels. *Front. Pharmacol.* **13**, 842032 (2022).
15. Tran, H. N. T. *et al.* Enzymatic Ligation of a Pore Blocker Toxin and a Gating Modifier Toxin: Creating Double-Knotted Peptides with Improved Sodium Channel NaV1.7 Inhibition. *Bioconjug. Chem.* **31**, 64–73 (2020).
16. Shen, H., Liu, D., Wu, K., Lei, J. & Yan, N. Structures of human Nav1.7 channel in complex with auxiliary subunits and animal toxins. *Science* **363**, 1303–1308 (2019).
17. Schmalhofer, W. A. *et al.* ProTx-II, a selective inhibitor of NaV1.7 sodium channels, blocks action potential propagation in nociceptors. *Mol. Pharmacol.* **74**, 1476–1484 (2008).
18. Xiao, Y., Blumenthal, K., Jackson, J. O., Liang, S. & Cummins, T. R. The tarantula toxins ProTx-II and huwentoxin-IV differentially interact with human Nav1.7 voltage sensors to inhibit channel activation and inactivation. *Mol. Pharmacol.* **78**, 1124–1134 (2010).
19. de Lera Ruiz, M. & Kraus, R. L. Voltage-Gated Sodium Channels: Structure, Function, Pharmacology, and Clinical Indications. *J. Med. Chem.* **58**, 7093–7118 (2015).
20. Wulff, H., Christophersen, P., Colussi, P., Chandy, K. G. & Yarov-Yarovoy, V. Antibodies and venom peptides: new modalities for ion channels. *Nat. Rev. Drug Discov.* **18**, 339–357 (2019).
21. Montnach, J. *et al.* Fluorescent- and tagged-protoxin II peptides: potent markers of the Nav1.7 channel pain target. *Br. J. Pharmacol.* **178**, 2632–2650 (2021).

22. Dutertre, S. & Lewis, R. J. Use of Venom Peptides to Probe Ion Channel Structure and Function. *J. Biol. Chem.* **285**, 13315 (2010).
23. Xu, H. *et al.* Structural Basis of Nav1.7 Inhibition by a Gating-Modifier Spider Toxin. *Cell* **176**, 702-715.e14 (2019).
24. Flood, E., Boiteux, C., Lev, B., Vorobyov, I. & Allen, T. W. Atomistic Simulations of Membrane Ion Channel Conduction, Gating, and Modulation. *Chem. Rev.* **119**, 7737–7832 (2019).
25. Deplazes, E. Molecular Simulations of Disulfide-Rich Venom Peptides with Ion Channels and Membranes. *Molecules* **22**, 362 (2017).
26. Henriques, S. T. *et al.* Interaction of Tarantula Venom Peptide ProTx-II with Lipid Membranes Is a Prerequisite for Its Inhibition of Human Voltage-gated Sodium Channel NaV1.7. *J. Biol. Chem.* **291**, 17049–17065 (2016).
27. Mateos, D. L. & Yarov-Yarovoy, V. Structural Modeling of Peptide Toxin - Ion Channel Interactions using RosettaDock. 2022.06.29.498146 Preprint at https://doi.org/10.1101/2022.06.29.498146 (2022).
28. Katz, D., Sindhikara, D., DiMattia, M. & Leffler, A. E. Potency-Enhancing Mutations of Gating Modifier Toxins for the Voltage-Gated Sodium Channel NaV1.7 Can Be Predicted Using Accurate Free-Energy Calculations. *Toxins* **13**, 193 (2021).
29. Catterall, W. A. Structure and function of voltage-gated sodium channels at atomic resolution. *Exp. Physiol.* **99**, 35–51 (2014).
30. Rohl, C. A., Strauss, C. E. M., Misura, K. M. S. & Baker, D. Protein structure prediction using Rosetta. *Methods Enzymol.* **383**, 66–93 (2004).
31. Mandell, D. J., Coutsias, E. A. & Kortemme, T. Sub-angstrom accuracy in protein loop reconstruction by robotics-inspired conformational sampling. *Nat. Methods* **6**, 551–552 (2009).
32. Stein, A. & Kortemme, T. Improvements to robotics-inspired conformational sampling in rosetta. *PloS One* **8**, e63090 (2013).
33. Gray, J. J. *et al.* Protein-protein docking with simultaneous optimization of rigid-body displacement and side-chain conformations. *J. Mol. Biol.* **331**, 281–299 (2003).
34. Wang, C., Bradley, P. & Baker, D. Protein-protein docking with backbone flexibility. *J. Mol. Biol.* **373**, 503–519 (2007).
35. Alford, R. F., Fleming, P. J., Fleming, K. G. & Gray, J. J. Protein Structure Prediction and Design in a Biologically Realistic Implicit Membrane. *Biophys. J.* (2020) doi:10.1016/j.bpj.2020.03.006.
36. Wang, R. Y.-R. *et al.* Automated structure refinement of macromolecular assemblies from cryo-EM maps using Rosetta. *eLife* **5**, (2016).
37. Song, Y. *et al.* High-resolution comparative modeling with RosettaCM. *Struct. Lond. Engl. 1993* **21**, 1735–1742 (2013).
38. Jo, S., Kim, T., Iyer, V. G. & Im, W. CHARMM-GUI: A web-based graphical user interface for CHARMM. *J. Comput. Chem.* **29**, 1859–1865 (2008).
39. Salomon-Ferrer, R., Case, D. A. & Walker, R. C. An overview of the Amber biomolecular simulation package. *WIREs Comput. Mol. Sci.* **3**, 198–210 (2013).
40. Huang, J. & MacKerell Jr, A. D. CHARMM36 all-atom additive protein force field: Validation based on comparison to NMR data. *J. Comput. Chem.* **34**, 2135–2145 (2013).
41. Klauda, J. B. *et al.* Update of the CHARMM All-Atom Additive Force Field for Lipids: Validation on Six Lipid Types. *J. Phys. Chem. B* **114**, 7830–7843 (2010).
42. Best, R. B. *et al.* Optimization of the Additive CHARMM All-Atom Protein Force Field Targeting Improved Sampling of the Backbone φ, ψ and Side-Chain χ1 and χ2 Dihedral Angles. *J. Chem. Theory Comput.* **8**, 3257–3273 (2012).
43. Jorgensen, W. L., Chandrasekhar, J., Madura, J. D., Impey, R. W. & Klein, M. L. Comparison of simple potential functions for simulating liquid water. *J. Chem. Phys.* **79**, 926–935 (1983).

44. Salentin, S., Schreiber, S., Haupt, V. J., Adasme, M. F. & Schroeder, M. PLIP: fully automated protein–ligand interaction profiler. *Nucleic Acids Res.* **43**, W443–W447 (2015).
45. Srinivasan, J., Cheatham, T. E., Cieplak, P., Kollman, P. A. & Case, D. A. Continuum Solvent Studies of the Stability of DNA, RNA, and Phosphoramidate−DNA Helices. *J. Am. Chem. Soc.* **120**, 9401–9409 (1998).
46. Kollman, P. A. *et al.* Calculating Structures and Free Energies of Complex Molecules: Combining Molecular Mechanics and Continuum Models. *Acc. Chem. Res.* **33**, 889–897 (2000).
47. Wang, C. *et al.* Calculating protein–ligand binding affinities with MMPBSA: Method and error analysis. *J. Comput. Chem.* **37**, 2436–2446 (2016).
48. Miller, B. R. I. *et al.* MMPBSA.py: An Efficient Program for End-State Free Energy Calculations. *J. Chem. Theory Comput.* **8**, 3314–3321 (2012).
49. Shirts, M. R. *et al.* Lessons learned from comparing molecular dynamics engines on the SAMPL5 dataset. *J. Comput. Aided Mol. Des.* **31**, 147–161 (2017).
50. Lu, Q. & Luo, R. A Poisson–Boltzmann dynamics method with nonperiodic boundary condition. *J. Chem. Phys.* **119**, 11035–11047 (2003).
51. Duan, L., Liu, X. & Zhang, J. Z. H. Interaction Entropy: A New Paradigm for Highly Efficient and Reliable Computation of Protein–Ligand Binding Free Energy. *J. Am. Chem. Soc.* **138**, 5722–5728 (2016).
52. Ylilauri, M. & Pentikäinen, O. T. MMGBSA As a Tool To Understand the Binding Affinities of Filamin–Peptide Interactions. *J. Chem. Inf. Model.* **53**, 2626–2633 (2013).
53. Roe, D. R. & Cheatham, T. E. I. PTRAJ and CPPTRAJ: Software for Processing and Analysis of Molecular Dynamics Trajectory Data. *J. Chem. Theory Comput.* **9**, 3084–3095 (2013).
54. Pettersen, E. F. *et al.* UCSF ChimeraX: Structure visualization for researchers, educators, and developers. *Protein Sci. Publ. Protein Soc.* **30**, 70–82 (2021).
55. Hou, T., Wang, J., Li, Y. & Wang, W. Assessing the Performance of the MM/PBSA and MM/GBSA Methods. 1. The Accuracy of Binding Free Energy Calculations Based on Molecular Dynamics Simulations. *J. Chem. Inf. Model.* **51**, 69–82 (2011).
56. Sun, H. *et al.* Assessing the performance of MM/PBSA and MM/GBSA methods. 7. Entropy effects on the performance of end-point binding free energy calculation approaches. *Phys. Chem. Chem. Phys.* **20**, 14450–14460 (2018).
57. White, S. H. & Wimley, W. C. Hydrophobic interactions of peptides with membrane interfaces. *Biochim. Biophys. Acta* **1376**, 339–352 (1998).
58. Guvench, O. & MacKerell, A. D. Comparison of protein force fields for molecular dynamics simulations. *Methods Mol. Biol. Clifton NJ* **443**, 63–88 (2008).
59. Branduardi, D. & Faraldo-Gómez, J. D. String method for calculation of minimum free-energy paths in Cartesian space in freely-tumbling systems. *J. Chem. Theory Comput.* **9**, 4140–4154 (2013).
60. Ahn, S.-H., Ojha, A. A., Amaro, R. E. & McCammon, J. A. Gaussian-Accelerated Molecular Dynamics with the Weighted Ensemble Method: A Hybrid Method Improves Thermodynamic and Kinetic Sampling. *J. Chem. Theory Comput.* **17**, 7938–7951 (2021).
61. Sheng, Y., Yin, Y., Ma, Y. & Ding, H. Improving the Performance of MM/PBSA in Protein–Protein Interactions via the Screening Electrostatic Energy. *J. Chem. Inf. Model.* **61**, 2454–2462 (2021).
62. Spiliotopoulos, D. *et al.* dMM-PBSA: A New HADDOCK Scoring Function for Protein-Peptide Docking. *Front. Mol. Biosci.* **3**, (2016).
63. Liu, X., Peng, L. & Zhang, J. Z. H. Accurate and Efficient Calculation of Protein–Protein Binding Free Energy-Interaction Entropy with Residue Type-Specific Dielectric Constants. *J. Chem. Inf. Model.* **59**, 272–281 (2019).